


OVERVIEW

Fluid mechanical modeling of the upper urinary tract

**Shaokai Zheng¹ | Dario Carugo² | Ali Mosayyebi³ | Ben Turney⁴ |
Fiona Burkhard⁵ | Dirk Lange⁶ | Dominik Obrist¹ | Sarah Waters⁷  |
Francesco Clavica¹**

¹ARTORG Center for Biomedical Engineering Research, University of Bern, Bern, Switzerland

²Department of Pharmaceutics, UCL School of Pharmacy, University College London, London, UK

³Bioengineering Sciences, Faculty of Engineering and Physical Sciences, University of Southampton, Southampton, UK

⁴Nuffield Department of Surgical Sciences, University of Oxford, Oxford, UK

⁵Department of Urology, Inselspital, Bern University Hospital, University of Bern, Bern, Switzerland

⁶The Stone Centre at Vancouver General Hospital, Department of Urologic Sciences, University of British Columbia, Vancouver, British Columbia, Canada

⁷Oxford Centre for Industrial and Applied Mathematics, Mathematical Institute, University of Oxford, Oxford, UK

Correspondence

Sarah Waters, Oxford Centre for Industrial and Applied Mathematics, Mathematical Institute, University of Oxford, Oxford OX2 6GG, UK.
Email: waters@maths.ox.ac.uk

Funding information

European Cooperation in Science and Technology, Grant/Award Number: CA16217; Swiss National Science Foundation, Grant/Award Number: IZCOZ0_182966

Edited by Jessica Lawler, Editor.

Abstract

The upper urinary tract (UUT) consists of kidneys and ureters, and is an integral part of the human urogenital system. Yet malfunctioning and complications of the UUT can happen at all stages of life, attributed to reasons such as congenital anomalies, urinary tract infections, urolithiasis and urothelial cancers, all of which require urological interventions and significantly compromise patients' quality of life. Therefore, many models have been developed to address the relevant scientific and clinical challenges of the UUT. Of all approaches, fluid mechanical modeling serves a pivotal role and various methods have been employed to develop physiologically meaningful models. In this article, we provide an overview on the historical evolution of fluid mechanical models of UUT that utilize theoretical, computational, and experimental approaches. Descriptions of the physiological functionality of each component are also given and the mechanical characterizations associated with the UUT are provided. As such, it is our aim to offer a brief summary of the current knowledge of the subject, and provide a comprehensive introduction for engineers, scientists, and clinicians who are interested in the field of fluid mechanical modeling of UUT.

This article is categorized under:

Cancer > Biomedical Engineering

Infectious Diseases > Biomedical Engineering

Reproductive System Diseases > Biomedical Engineering

This is an open access article under the terms of the Creative Commons Attribution License, which permits use, distribution and reproduction in any medium, provided the original work is properly cited.

© 2021 The Authors. WIREs Mechanisms of Disease published by Wiley Periodicals LLC.

KEYWORDS

fluid mechanics, modeling, stent, urinary obstruction, urinary tract

1 | INTRODUCTION

The upper urinary tract (UUT) consists of the kidneys and ureters. Its primary function is to collect and transport urine to the bladder, where it is stored and excreted periodically to eliminate biological waste from the human body (Elbadawi, 1996; Fowler et al., 2008; Hickling et al., 2015). The functioning and performance of the UUT underpins the integrity of the human urogenital system, having a significant impact on individual health and well-being. Malfunctions and complications of the UUT can happen at all stages of life, for reasons such as congenital anomalies, urinary tract infections (UTIs), urolithiasis (i.e., urinary stones), and cancers (e.g., kidney cancer and ureteral cancer), all of which require urological interventions. This has motivated the development of many models to gain insight into the various physiological and pathological characteristics of the UUT to address scientific and clinical questions.

Of all approaches, fluid mechanical modeling serves a pivotal role in the study of the UUT. The primary fluid medium within the UUT is urine, whose behavior is governed by well-known fluid mechanical principles, and faithful modeling of the flow environment underpins (mechano-)biological investigations of the UUT. Over the past few decades, a number of theoretical, computational, and experimental efforts have contributed to the realization of anatomically and physiologically meaningful models, and the methodologies adopted by these works are of archival value.

In this article, we focus on the historical evolution of fluid mechanical models of the UUT derived via complementary approaches. To elucidate the basis of all modeling work, we first summarize the physiological and mechanical characterizations of the UUT, and provide the parameter values required to calibrate any fluid mechanical model. Subsequent discussions are divided into three sections based on each modeling approach, that is, reduced order methods, computational methods, and experimental methods. As such, we aim to provide a comprehensive overview of the subject for engineers, scientists, and clinicians interested into fluid mechanical modeling of the UUT, calling forth new perspectives to go beyond the status quo.

2 | PHYSIO-MECHANICAL CHARACTERIZATIONS

The UUT is a multi-organ and dynamic system, which requires a large number of parameters to fully describe its mechanical and physiological characteristics. Clinically relevant models depend on selecting physiologically meaningful values for each associated parameter. In this section, we present physiological values from the literature for the fundamental mechanical parameters of the UUT (e.g., geometries, pressures, and flow rates), and briefly discuss the physio-mechanical characteristics of each organ. Note that, all values are taken from the human UUT unless otherwise stated.

2.1 | Kidneys

The kidneys are responsible for the production and collection of urine. Each kidney contains around one million functional units (nephrons) that amass urine through a branched collecting system that drains into the renal calyces. All calyceal branches connect to the renal pelvis, and the ureteropelvic junction (UPJ) connects the renal pelvis to the proximal (i.e., close to the kidney) ureter (Figure 1(a)). Mechanical and mathematical characterization of renal physiology have been reviewed by Bykova and Regirer (2005) and Spirka and Damaser (2007), where the circulation of blood and mass transfer in the nephron are discussed. In the current context, that is, to study the urine flow within the UUT, the kidney is often treated as a boundary condition (BC) for the ureter, where the intraluminal renal pelvic pressure (RPP) and inlet flow rate are most relevant parameters.

The actual value of the RPP averages about 12–15 cm H₂O (Rattner William et al., 1957; Walzak & Paquin, 1961), and is generally considered to be below 20 cm H₂O for healthy individuals. The urine production rate has been shown to vary between 0.3 and 2.4 ml/min for each kidney (Ohlson, 1989), and might be significantly higher for people with pathological conditions such as polyuria and diabetes mellitus.

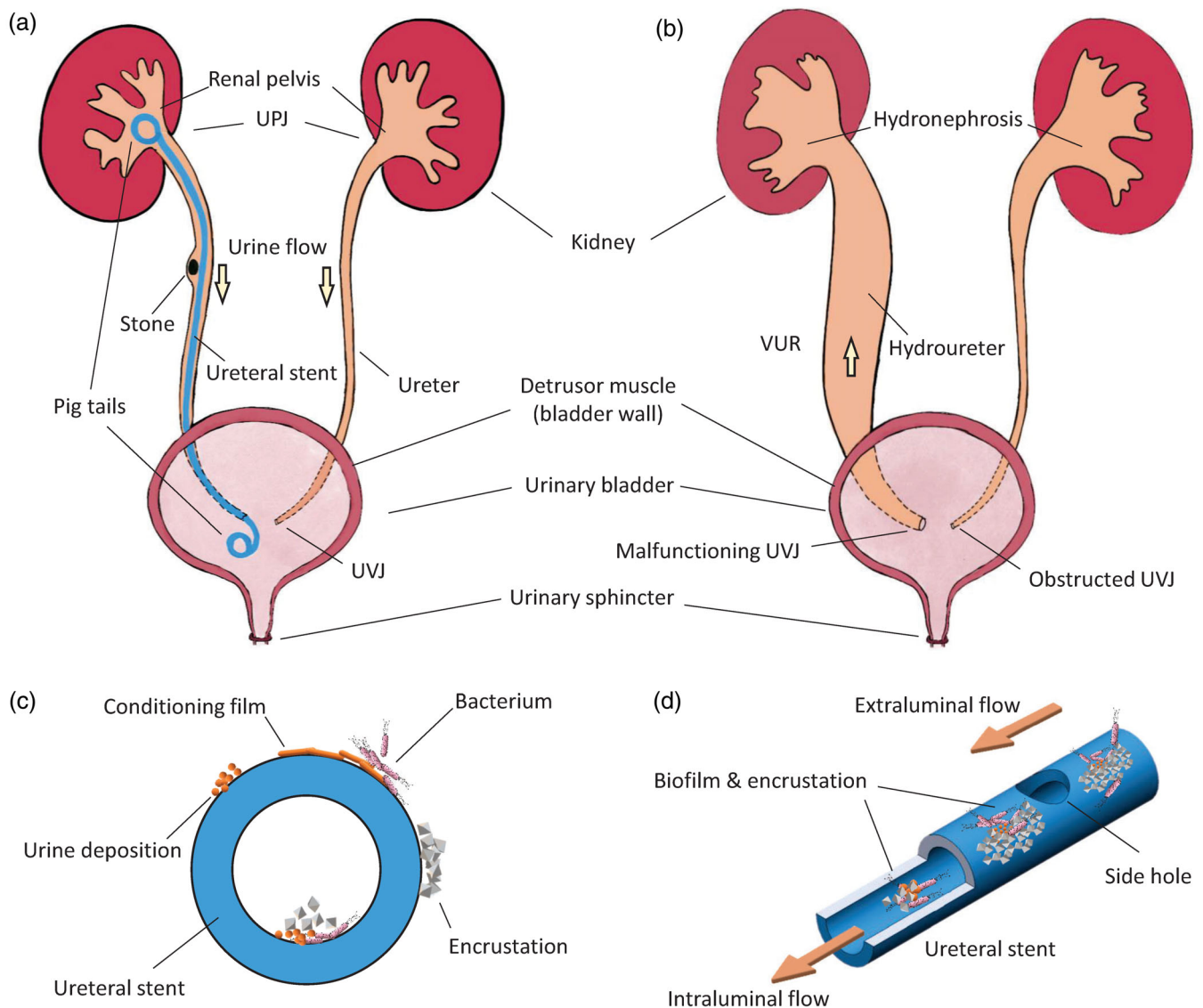


FIGURE 1 Illustration of the urinary tract under various physiological and pathological conditions. (a) On the left: a ureter obstructed by an urinary stone and implanted with a Double-J (DJ) stent to maintain drainage. The two pigtails are situated in the renal pelvis and bladder, respectively. On the right: a healthy ureter. (b) On the left: a ureter with congenital ureterovesical junction (UVJ) malfunction, causing primary vesicoureteral reflux (VUR). The VUR, which is the retrograde ascension of urine flow, may induce hydroureter and hydronephrosis. On the right: a ureter with congenital UVJ obstruction, which impedes the drainage of urine and leads to hydronephrosis. (c) Cross sectional view of the ureteral stent. Stages of biofilm and encrustation formation are illustrated on the stent surface. (d) Three dimensional view of the ureteral stent showing a side hole, which is designed to promote exchange between intraluminal (within the lumen of the stent) and extraluminal (between the external surface of the stent and the ureter wall) urinary flows. Structures comprising both biofilm and encrustation can be formed on both internal and external surfaces of the stent, causing further complications for patients

In terms of relevant dimensions, in a study of 665 adults from 30 to 70 years old (Emamian et al., 1993), 87% of the subjects have transverse diameters of the renal pelvis smaller than 10 mm. The lower limit is not reported, but the average transverse diameter of the fetal renal pelvis (12–25 weeks) has been reported as 3.6 mm (Lobo et al., 2011). The anteroposterior diameter of renal pelvis measures approximately 5 mm at age 18–19, with an upper limit (95 percentile) of 15 mm (Chitty & Altman, 2003; Schaeffer et al., 2016). In the presence of obstruction and subsequent hydronephrosis, the anteroposterior diameter can reach up to 21–38 mm with patient age between 6 weeks and 16 years (Mesrobian, 2009). In the context of fluid mechanical modeling, the renal pelvis is usually treated as a solid boundary, and it is physiologically reasonable to assume a circular cross section of approximately 10 mm in diameter. In the case of oncological patients, tumor growth in the kidney will dynamically alter the regional tissue composition

and the geometry of UUT, which will in turn affect its fluid mechanical performance. Thence, the material properties of the renal pelvis, such as Young's modulus and Poisson ratio, should be considered when modeling certain physio-pathological conditions (Chen et al., 2013).

2.2 | Bladder

The urinary bladder, or simply bladder, is considered as part of the lower urinary tract (LUT), and has been examined quite extensively in urodynamic studies to diagnose and better understand LUT symptoms. In the context of UUT modeling, the bladder compartment is typically introduced as a BC, and its storage volume and pressure profiles are of primary interest.

The bladder is a hollow, distensible organ, which receives urine drained from both ureters and voids periodically (referred to as micturition) through the urethra. The storage volume of bladder varies largely between individuals, but is generally assumed to be around 500 ml (Bykova & Regirer, 2005). According to a retrospective study of 976 urodynamic records from individuals with no pathological conditions, the voided volume averages at 508 (± 225) ml for males and 468 (± 203) ml for females, which is an indication of the bladder capacity (Alou's et al., 2010). Further, the bladder capacity has been reported to decrease with age, and can be affected by other diseases (Dionne Ananias et al., 1987). Notably, there is often a small postvoid residual urine volume in the normal bladder. The postvoid volume is generally smaller than 50 ml (Alloussi et al., 2010), and increased residual volumes can cause urinary tract infections (the larger the volume the higher the risk).

The bladder wall is comprised of smooth muscle fibers oriented in different directions. These smooth muscles are collectively known as the detrusor muscle. The true bladder pressure is usually defined as the detrusor pressure, which is calculated by subtracting the intra-abdominal pressure (IAP) from the intravesical pressure (IVP). From conventional urodynamic tests, the IAP is usually taken as the intrarectal pressure, measured with a catheter inserted at least 10 cm into the rectum (McCarthy, 1982). The IVP is the pressure inside the bladder, which is usually measured with a catheter inserted through the urethra. The normal IAP at rest averages at about 8 cm H₂O for healthy individuals, and increases to higher baseline levels from supine to standing position (Schäfer et al., 2002). The baseline IAP is also reportedly higher for morbidly obese patients (De Keulenaer et al., 2009).

The detrusor pressure varies during the two defined stages of bladder function, that is, the filling phase, and the voiding phase. The viscoelastic properties of the bladder wall allow for increases in bladder volume with little change in detrusor pressure. During the filling phase, the detrusor muscle stays relaxed, and the detrusor pressure remains small (roughly between 2 and 5 cm H₂O). During the voiding phase, the detrusor muscle contracts, causing a rise in detrusor pressure especially in men due to the greater hydraulic resistance offered by the prostate. In the retrospective study of Alloussi et al. (2010), the detrusor pressure at maximum flow rate during micturition is reported as 38.3 (± 11.5) cm H₂O for males and 32 (± 10.6) cm H₂O for females, with averaged (peak) flow rates through the urethra higher than 24 ml/s.

A final consideration about bladder physiology relates to its temporal dynamics, which is linked to the urine production rate, and the outflow rate through the urethra. The duration of the filling phase varies largely with the activity of the individual, and can be easily accelerated (decelerated) by increasing (decreasing) the fluid intake. For healthy individuals, the voiding time has been reported to be around 40 s (Alloussi et al., 2010), provided that both bladder capacity and voiding flow rate are within the normal range.

2.3 | Ureters

The ureters are long collapsible fibromuscular tubes that pass urine from the kidneys to the bladder. The proximal ureter starts at the UPJ, and the distal (i.e., close to the bladder) ureter obliquely enters the bladder wall at the ureterovesical junction (UVJ). The ureter passes through the detrusor muscle and travels submucosally for 1.5–2 cm before entering the bladder lumen at the ureteral orifice (Hickling et al., 2015). This creates a valve-like mechanism when the IVP is applied to the UVJ, preventing urine from flowing back up into the ureter (Juskiewenski et al., 1984).

The length of the ureter is approximately 22–30 cm (Hickling et al., 2015), and its diameter varies from 1 to 6 mm with an average of 1.8 mm as measured 1–2 cm below the UPJ (Zelenko et al., 2004). The diameter is physiologically smaller at the UPJ, UVJ, and where the ureters turn medially and cross the common iliac vessels. In the case of

urolithiasis with obstruction, the diameter has been shown to vary between 1 and 20 mm with an average of 7 mm (Zelenko et al., 2004), but could potentially exceed this range depending on the pathological condition.

The intraluminal pressure of the ureter is similar to that of the renal pelvis in healthy ureters, averaging at 13.5 cm H₂O in midureter, and 13 cm H₂O in the lower third of the ureter (Rattner William et al., 1957). These values can be substantially increased in presence of an obstruction (either internal or external) or implanted stent (Cormio et al., 1994; Rattner William et al., 1957; Shao et al., 2009). In some cases, urine flow is modeled as a pressure driven flow with fixed BCs, such that the pressure difference between UPJ and UVJ is prescribed. Considering the values given above, the pressure difference, that is, subtracting IVP from RPP, falls in the order of 2 cm H₂O during the filling phase.

Regarding the structural properties of the ureter, the cross section of contracted human ureter resembles a stellate shape. The thickness of the ureter wall, including epithelium, lamina propria, and muscularis, measures about 1 mm (Wolf et al., 1996). However, it significantly thickens and stiffens with age (Sokolis, 2020; Sokolis et al., 2017). In various UUT studies, ureters are often simplified to straight circular tubes, neglecting the stellate lumen shape.

Finally, to model the compliance of the ureter wall, the distensibility becomes relevant, which is defined as the change in diameter due to the intraluminal pressure (Equation 12), and it has been reported as 2 cm H₂O/mm (Griffiths, 1987). The reported elastic modulus of human ureter is 3.48 ± 0.47 MPa along the longitudinal direction, and 2.31 ± 0.46 MPa in the circumferential direction (Rassoli et al., 2014). These values are important to model the wall dynamics of the ureter, especially in the presence of peristaltic waves.

2.4 | Ureteral peristalsis

In the human ureter, smooth-muscle cells located near the renal pelvis (Figure 1(a), (b)) border are thought to act as the pacemakers of ureter peristalsis, which is a traveling contraction wave that drives the flow of urine from the kidneys to the bladder (Rasouly & Lu, 2013). These waves are mostly monophasic, traveling at speeds of approximately 2–3 cm/s, and are typically 6–10 cm in length (Griffiths, 1987, 1989). The peristaltic wave happens about 1–8 times per minute in normal human, and averages about three times per minute (Edmond et al., 1970; Weinberg & Maletta, 1961). According to the measurement taken from 17 healthy adult females, the maximum pressure amplitude averages 17.5 cm H₂O in the midureter, and 22 cm H₂O in the lower ureter (Rattner William et al., 1957). From other studies (i.e., Griffiths, 1987, 1989; Weinberg & Maletta, 1961), this peak pressure value varies between 15 and 50 cm H₂O in normal humans, and is generally larger toward the lower part of ureter.

Note that the ureteral peristalsis is strongly affected by the presence of an implanted ureteral stent, even ceasing completely, as concluded from several experiments using porcine models (Kinn & Lykkeskov-Andersen, 2002; Venkatesh et al., 2005). Retrograde peristalsis, aberrant waves, and incomplete contractions have all been reported. In the study by Venkatesh et al. (2005), all peristaltic movements were stopped regardless of the stent size. Due to the anatomical similarity between porcine and human UUT (Sampaio et al., 1998), it is reasonable to conclude that the same applies to the human UUT. In fact, Mosli Hisham et al. (1991) reported that for patients with indwelling double-pigtail stents the peristaltic waves were sluggish and averaged to 1–2 waves per minute. Therefore, it is common to neglect the peristalsis in fluid mechanical models of stented ureter, especially in experimental investigations. A summary of the values of various parameters used in previous models associated with the ureter is given in Tables A2 and A3 for reference.

2.5 | Ureteral stent

Ureteral stents, as an integral part of modern urologist's armamentarium, are indispensable devices often used to drain UUT in the case of obstruction or to avoid obstruction after an intervention as a complement to Shock Wave Lithotripsy (SWL) or kidney transplant (Haleblian et al., 2008). In spite of their common use and various design upgrades since their first introduction in the 1960s (Donahue et al., 2018; Khoo et al., 2018; Mosayyebi, Manes, et al., 2018; Zimskind Paul et al., 1967), pain, bladder irritation, flank pain due to reflux, and sexual dysfunction associated with implanted stents significantly compromise patients' quality of life (Ringel et al., 2000; Shaw et al., 2005), and may cause serious infections (Scotland et al., 2019). For some patients, such as those with advanced malignant obstruction, or those not fit for definitive surgery, long-term stenting is required. The usual maximum lifespan of an indwelling long-term ureteral

stent is approximately 6 months. However, the real lifespan is often reduced due to a range of complications, which include biofilm formation and infection, obstruction and encrustation. These necessitate more frequent stent replacements, sometimes every few weeks, which is inconvenient for the patient and places an increased burden on the healthcare system. The development of biofilm and encrustation on stent surfaces (Figure 1(c), (d)) therefore remains one of the most challenging topics in both research and clinical studies of the UUT (Ramachandra et al., 2020; Ramstedt et al., 2019; Sali & Joshi, 2020), and UUT models are often developed to investigate aspects of ureteral stents and their performance.

The state-of-the-art ureteral stents are polymer stents about 24–32 cm in length and 1–2 mm in outer diameter with a circular cross section. Other cross-sectional shapes have also been documented such as multiple shallow grooves on the surface or a three- or four-edged stellate shape (Birch et al., 1988). They usually feature pigtailed ends on each end (Figure 1(a)) as a feature to prevent dislocation, and side holes are often distributed along the whole length of the stent to promote the exchange of intraluminal and extraluminal flows (Figure 1(d)), although the efficacy of side holes is still debatable.

As an alternative to polymer stents, metallic stents are sometimes favored in the case of extrinsic ureteral compression for their higher tensile strength (Hendlin et al., 2012; Khoo et al., 2018). In recent years, research into biodegradable stents has become more active (Barros et al., 2018; Soria et al., 2018; Zhu et al., 2017), driven by the need to eliminate the problem of forgotten stents and reduce the number of hospital visits. The current investigations are however primarily focused on the material degradation and stent migration as the stent dissolves. To the best of the authors' knowledge, there is no available report on the fluid mechanical performances of biodegradable stents over time.

To study the performance of stents in a systematic way, various models have been deployed to date under different assumptions. Generally, bench-top in-vitro models allow rapid testing for a range of clinical scenarios, where stents of various material properties and geometries can be tested as is with minimal assumptions. In comparison, both reduced order models and computational models treat indwelling stents as rigid, circular, and hollow tubes. Generally, the geometry and configuration of side holes are faithfully replicated in computational models, and simplified to permeable walls in reduced order models. A summary of the stent parameters previously investigated in UUT models is given in Table A4 for reference.

Furthermore, to evaluate the impact of indwelling time on stent integrity and drainage performance, the material property of stents (especially its variation over time) becomes relevant (Arkusz et al., 2020). Such variation depends not only on the material fatigue caused by body movements, but also on the chemical composition of urine, which promotes the development of biofilm and encrustations and potentially compromises the integrity of the stents (Shilo et al., 2020).

2.6 | Urine

Human urine is not sterile. As a biological waste, it typically contains a wide range of metabolic breakdowns from food, drinks, drugs, and so on, as well as bacterial by-products (Tang, 2017). As a result, the mechanical properties and chemical composition of urine incorporate both intrasubject and intersubject variability. Artificial urine (AU) is therefore often used as the working fluid for most modeling studies to ensure reproducibility. Recipes of AU compositions can be found in Greenwood and O'Grady (1978), Tunney et al. (1996), Schlick and Planz (1998), Mosayyebi, Manes, et al. (2018), Khandwekar and Doble (2011), Barros et al. (2015), Cauda et al. (2017).

The mechanical properties of AU are similar to that of water (and normal urine) with a density of approximately 1 g/cc and dynamic viscosity of 0.01 g/(cm s), and are generally taken as constant. If temperature effects are of interest, the previously reported monotonic variation of kinematic viscosity from 0.011 g/(cm s) at 37°C to 0.007 g/(cm s) at 42°C might be considered (Inman et al., 2013). The working temperature for AU is generally set to be within 35–40°C to simulate the human environment (Cauda et al., 2017, Choong et al., 2000, Chua et al., 2017, Mosayyebi, Manes, et al., 2018, Mosayyebi, Yue, et al., 2018). The pH value of normal human urine averages around 6 (Tang, 2017), and various studies have prescribed pH values between 5 and 9 (Chua et al., 2017; Hobbs et al., 2018; Schlick & Planz, 1998) to study the chemical or biological characteristics of urine. Table A5 summarizes the parameters of (artificial) urine previously used in various UUT models.

2.7 | Pathological changes

The UUT is subject to a range of congenital anomalies and acquired pathological conditions. As such, the physio-mechanical characterization of the UUT is subject to differences in terms of topology, pressure, material properties, and

so on. This section discusses some of the common conditions and briefly points out the possible changes of various parameters resulting from anomalies and pathological conditions in a qualitative manner.

Congenital anomalies of the UUT are one of the major concerns among pediatric urology. Common anomalies of the ureter and associated junction structures (e.g., ureterocele) ultimately leads to abnormal urine transport such as obstructions and primary vesicoureteral reflux (VUR), which is the retrograde ascension of urine from bladder back into the ureters. These conditions eventually cause dilation of the renal pelvis (i.e., hydronephrosis) and the affected ureters (i.e., hydroureter or megaureter), as illustrated in Figure 1(b). In such cases, both the change of the junction structure (e.g., restricted opening) and the increase of intraluminal pressure in the UUT need to be considered.

Acquired pathological conditions such as urolithiasis (Figure 1(a)) and upper tract tumors can both impede the normal transport of urine in the UUT, and often require long-term stenting. In the presence of indwelling stent, the normal peristalsis of the ureter wall is reduced or stopped, and the intraluminal pressure is considerably increased (Shao et al., 2009). Furthermore, the presence of stent prevents the UVJ from closing properly and causes secondary VUR (Mosli Hisham et al., 1991), which in turn leads to increased pressures in the ureter and renal pelvis. Notably, due to the extra resistance caused by prostate in male patients, the detrusor pressure during voiding is usually higher than that of women. Therefore, men are more likely to feel the reflux, which is often associated with pain.

Another crucially important issue is the development of biofilm and encrustations over time on the surfaces of inserted urological devices. As the foreign materials are in contact with urine, a layer of absorbed biological substances forms on the material surfaces, referred to as the conditioning film. This film alters the surface roughness and topology of the stent, facilitating adhesion and colonization of various microparticles and microorganisms (Ramstedt et al., 2019; Scotland et al., 2019). This process eventually leads to the formation of biofilm and encrustations on material surfaces (Figure 1(c)). As the biofilm and encrustation grow, the intraluminal flow can be completely hindered (Figure 1(d)). With increasing population of microparticles and microorganisms, the Newtonian viscous fluid model of urine fails, and multiphase, non-Newtonian formulations might be more appropriate (Chrispell & Fauci, 2011; Jiménez-Lozano et al., 2011; Riaz & Sadiq, 2020).

3 | REDUCED ORDER METHODS

One approach to develop theoretical models of the fluid inside a (stented) ureter is to exploit the disparate length scales inherent in the system to obtain reduced models that retain the key physics, but are simpler to solve than full computational models. These models can be used to reveal the underlying mechanisms of the system, and complement full computational simulations in anatomically realistic geometries.

In this context, lubrication theory is often exploited to derive reduced models of the UUT. The use of lubrication theory is motivated by the small aspect ratio of the ureter (i.e., ratio of radius to length is small) and small Reynolds number which allows fluid inertia to be neglected (Carew & Pedley, 1997; Cummings et al., 2004; Lykoudis & Roos, 1970; Roos & Lykoudis, 1971). In the lubrication regime, the flow is predominantly in the axial direction, and the pressure does not vary in the transverse direction. The model geometry is often taken to be axisymmetric or 2D Cartesian.

In most fluid mechanical models of the UUT, the urine is typically modeled as an incompressible Newtonian fluid. Such flow is governed by the continuity equation and the Navier–Stokes (N–S) equations. For the axisymmetric case (no variation in the azimuthal direction and no azimuthal flow), the governing equations are given in the cylindrical polar coordinate system as

$$\begin{aligned}
 \frac{\partial w}{\partial z} + \frac{1}{r} \frac{\partial(ru)}{\partial r} &= 0 \\
 \frac{\partial p}{\partial z} &= \frac{\mu}{r} \frac{\partial}{\partial r} \left(r \frac{\partial w}{\partial r} \right) \\
 \frac{\partial p}{\partial r} &= 0
 \end{aligned} \tag{1}$$

where (z, r) are the axial and radial coordinates with corresponding velocity components (w, u) , μ is dynamic viscosity, and p is the fluid pressure. The governing equations must be solved subject to appropriate BCs.

Lykoudis and Roos (1970), and Roos and Lykoudis (1971) derived perhaps the earliest reduced order models for the UUT. They modeled the healthy ureter as an axisymmetric tube, and peristalsis of the ureter wall by prescribing the local shape of the ureter wall distal to the collapse as $r = h(z - ct)$, where $h \sim z^n$ is a polynomial function of z , n is an arbitrary constant ($n \geq 1$), and c is the speed of the traveling wave (as shown in Figure 2(a)). In a Lagrangian axisymmetric coordinate system moving with the wave speed c , the wave appears stationary and the wall moves leftward with speed c . The governing Equations (1) are solved subject to:

$$w = -c \text{ at } r = h(z), \quad (2)$$

$$\frac{\partial w}{\partial r} = 0 \text{ at } r = 0, \quad (3)$$

$$u = 0 \text{ at } r = 0. \quad (4)$$

When a catheter is inserted into the ureter (Roos & Lykoudis, 1971), the governing Equations (1) become subject to $w = -c$ at $r = h(z)$, $w = -c$ at $r = a$, and $u = 0$ at $r = a$, where a is the radius of the catheter and $a \leq b$, b being the ureter radius in the collapsed state (Figure 2(a)).

While Roos and Lykoudis (1971) and Lykoudis and Roos (1970) considered the pressure distribution within the ureter due to prescribed peristaltic waves of the ureter wall, their model neglected the bladder and kidney. As a result, a major limitation of these models is that they cannot be used to describe clinical conditions such as reflux. Additionally, material properties of the stent, ureter walls, and so on are overlooked. This was remedied by Cummings et al. (2004),

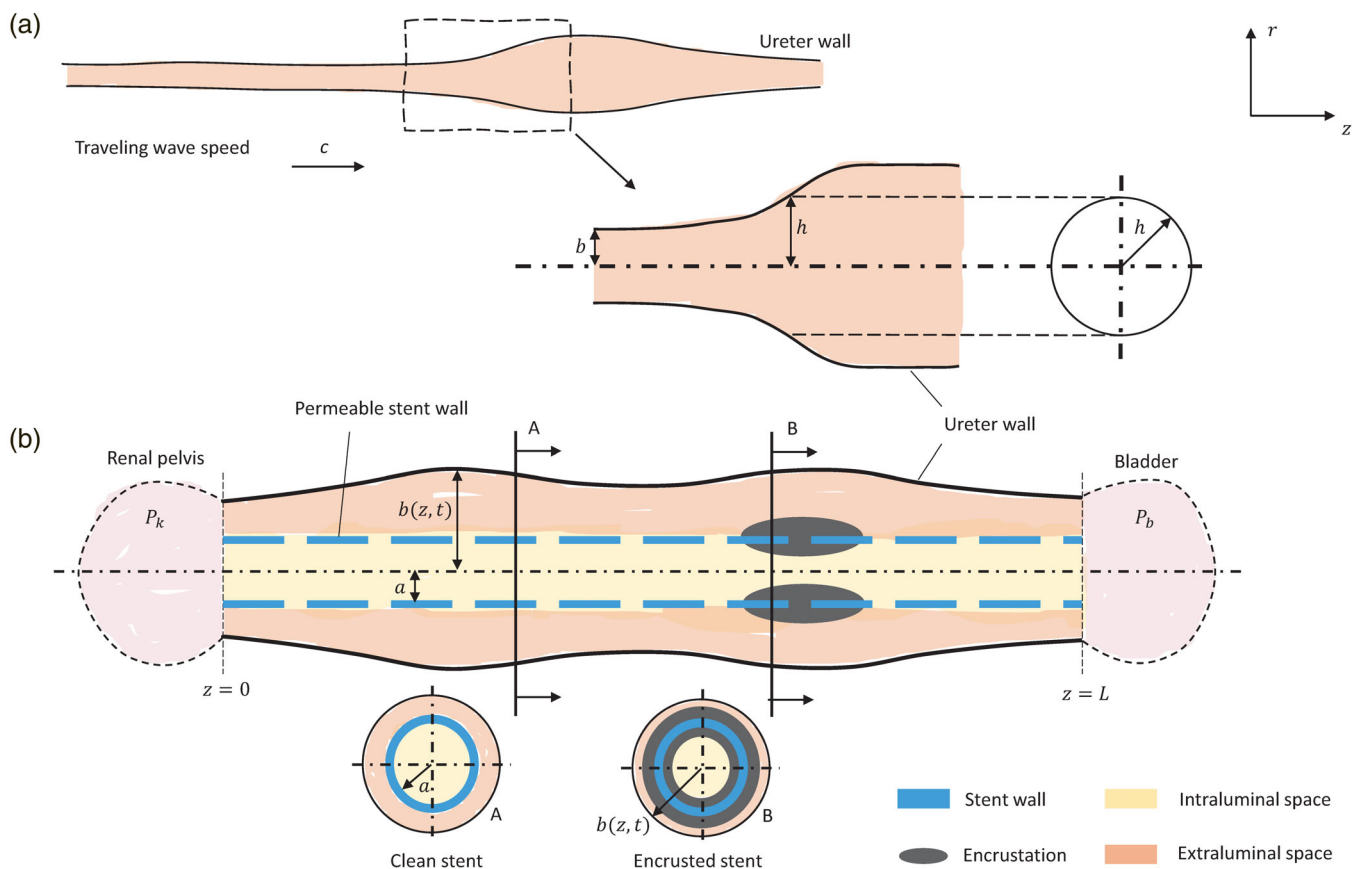


FIGURE 2 Schematic sketch for the general setup of reduced models. Different parts of the urinary tract are color coded. (a) Unstented ureter with travelling waves, and the geometry of the reduced ureter model (Lykoudis & Roos, 1970), where c is the wave speed of the peristaltic wave, b is the radius of the occluded ureter, h is the local radius of the expanded ureter. (b) Stented ureter with prescribed renal pelvis and bladder pressures (P_k and P_b , respectively) as BCs (Cummings et al., 2004; Siggers et al., 2009). The stent is modeled with permeable walls to incorporate the effect of side holes. Encrustations are also included by the local variation of stent geometry

who proposed the subsequent model to study reflux within stented ureters. The setup of the model is shown in Figure 2 (b). In this case, the fluid domain consists of the fluid inside the stent (intraluminal), and the fluid between the stent and the ureter wall (extraluminal). One of the advantages of this model is the inclusion of side holes by assuming constant permeability λ of the stent wall. Scenarios with different number of side holes on the stent can be modeled by varying the permeability. The BCs state that the inner and outer radial velocities across the stent wall are equal, and no-slip conditions are enforced (no tangential velocity) on either side of the stent walls, that is,

$$\begin{aligned} w_i &= w_e = 0, \\ u_i &= \lambda(p_e - p_i) = u_e, \end{aligned} \quad \text{at } r = a, \quad (5)$$

where the subscript i and e denote intraluminal and extraluminal flow, respectively, and a is the radius of the stent. Note that, p_i and p_e are reduced pressures, where the effect of gravity and ambient body pressure are removed (Cummings et al., 2004; Siggers et al., 2009).

Furthermore, to model the compliant ureter, Cummings et al. (2004) introduced a stiffness function $k(z)$, which quantifies how difficult it is to stretch the ureter radially. The dependence on z allows variations in the local stiffness values to model physiological conditions such as obstruction, where the local stiffness is large. The ureter wall is then modeled using a linear elastic model, such that

$$k(z)[b(z, t) - b_a(z)] = p_i, \quad \text{for } p_i > 0 \quad \text{at } r = b, \quad (6)$$

where $b(z, t)$ is the internal radius of the ureter as a function of axial location z and time t , and $b_a(z)$ is the radius of the ureter at ambient state (note, however, this is a linear approximation of the nonlinear wall). Based on the previous study of Knudsen et al. (1994), the stiffness can be estimated as $k = 41 \text{ cm H}_2\text{O}/\text{mm}^2$.

The axial BCs are given by the reduced renal pelvis pressure P_k and the bladder pressure P_b , which are non-dimensionalized to remove the ambient body pressure (i.e., IAP) and the effect of gravity. Having determined the flow field, the reflux volume (i.e., flow volume of VUR) can be evaluated by integrating the resulting velocity field over the modeled domain within the ureter.

Following this, Waters et al. (2008) improved their previous model (Cummings et al., 2004) by including the nonlinear elastic properties of the ureter wall. They performed a systematic investigation of the correlation between the pressure pulses in the bladder and the resulting VUR volume in the ureter. In this model, the ureter wall is modeled as elastic membrane with natural (unstretched) cross-sectional area A that expands only in the radial direction (neglecting axial stretch), and the tension is assumed to be a nonlinear function (Fung, 1967) of the radial stretch $f(\lambda) = k(e^{\alpha(\lambda - 1)} - 1)$, where λ is the ratio between the strained and unstrained ureter diameter, k is the stiffness of the wall, and α is a positive constant describing how rapidly the membrane tension varies with ureter radius ($\alpha = 1$ is usually accepted). As such, $f(1) = 0$ denotes zero stress in the relaxed state. The wall inertia is also neglected since the time scale over which the ureter wall achieves equilibrium is much smaller compared to that of the flow. This work also included the renal pelvis as an elastic bag of constant bulk stiffness k_r and pressure $P_r(t)$, a function of time t . The pressures at the two ends of the ureter are then taken as those in the renal pelvis and bladder, respectively. The renal pelvis pressure is defined as the sum of equilibrium pressure plus the pressure caused by the volume expansion, that is, $P_r = P_{r, \text{stat}} + k_r \Delta V$, where k_r is the bulk stiffness. The governing equations, after nondimensionalization, are reduced to two equations

$$\frac{\partial A}{\partial t} + \frac{\partial Q}{\partial z} = 0, \quad (7)$$

$$\frac{\partial^2 P_s}{\partial z^2} = d(P_s - P_u), \quad (8)$$

where A is the ureter cross-sectional area, Q is the total urine flux within the ureter, P_s is the pressure within the stent, and P_u is the pressure in the extraluminal space (Siggers et al., 2009). The pressure values, P_s and P_u , are set to zero initially, when the fluid is stationary and the ureter cross section area is equal to A . The rise and subsequent fall back of

bladder pressure due to voiding (or spasms) is then modeled dynamically as $P_b = P_{b,\max} \sim \sin^2(\pi t/T)$, where $P_{b,\max}$ is the maximum bladder pressure, and T is the duration of bladder activity. Consequently, the BCs are given as

$$\begin{aligned} P_s &= P_u, \\ \partial P_u / \partial t &= -k_k Q, \quad \text{at } z=0, \end{aligned} \quad (9)$$

$$\begin{aligned} P_s = P_u = P_b(t) &= \sin^2(\pi t), \quad 0 \leq t \leq T, \\ P_s = P_u = P_b(t) &= 0, \quad t > T, \end{aligned} \quad \text{at } z=L. \quad (10)$$

With this model, different cases of the pressure wave pulses (extreme values and pulse duration) can be examined in relation to the volume of VUR. Their results demonstrated a strong positive correlation between the VUR volume and pulse duration and increasing peak bladder pressure. The authors argue that the VUR exacerbates stent encrustation by bringing the bladder urine (which has a higher concentration of salt) and bacteria back to the ureter and renal pelvis.

Siggers et al. (2009) extended the model of Cummings et al. (2004) to incorporate urine production by the kidney (with a prescribed flux), and axial variations of the stent wall thickness due to encrustations (local variations of stent radius, as shown in Figure 2(b)), while other properties of the ureter wall, stent and BCs remained the same. Two types of bladder pressure pulses were prescribed to model bladder spasms and bladder voiding with triangular (spasm) and trapezoid (voiding) pressure waves, respectively. Their results confirm that the total reflux is proportional to the pressure elevation inside the bladder, and that the functionality of the UVJ is important in preventing reflux. This model would allow investigations of VUR and bladder physiology in a quantitative manner, which is clinically relevant considering the paucity of VUR data.

In contrast to the axisymmetric models discussed above, Griffiths and colleagues studied the pressure flow within collapsible tubes of finite length (Griffiths, 1985, 1987, 1989; Griffiths et al., 1987). This model assumes that the tube is uniform in shape and the axial rate of change of s remains relatively small. The fluid pressure is related to the wall mechanics via the tube law

$$p = p_{\text{pas}}(s) + p_{\text{act}}(s, z - ct), \quad (11)$$

where p_{pas} is the passive contribution that depends only on the wall separation s , and p_{act} is the active contribution that depends on the contraction of the ureter muscular wall traveling at axial velocity or wave speed c . The active pressure wave p_{act} is symmetrical and triangular in form with a total length of $2l$ and a peak value of p_{max} . Linear relations of the pressure distribution is then assumed such that

$$dp_{\text{pas}}/ds = \gamma, \quad \partial p_{\text{act}}/\partial s = 0, \quad (12)$$

$$\partial p_{\text{act}}/\partial z = \pm p_{\text{max}}/l, \quad (13)$$

where γ is the distensibility of the passive ureter, p_{max} is the maximum amplitude of the active contraction wave, and $2l$ is the total length of the active wave. By varying the peristalsis frequency, and hence the mean flow rate, four different types of solutions are obtained. Two of these solutions, that is, isolated fluid boluses and boluses in contact, are steady solutions similar to those proposed in the 1970s. The fluid pressure is maintained at a low value and the kidney is isolated from modest changes in bladder pressure. The other two unsteady solutions are attributed to the finite tube length, that is, leaky bolus flow and open tube flow, in which the boluses are less well defined and the contraction waves are in general not completely occlusive. These two types of solutions happen at higher mean flow rates, such that the fluid pressure exceeds the tube pressure and forces the collapsed ureter to open. As such, the peristaltic contractions of the ureter may even hinder the urine flow.

Last but not least, it is worth pointing out that urine has also been modeled as a multiphase fluid and/or non-Newtonian fluid in several studies using reduced order methods to address pathological changes of urine (Jiménez-Lozano, 2009; Jiménez-Lozano et al., 2011; Jiménez-Lozano & Sen, 2010; Rath & Reese, 1984; Riaz & Sadiq, 2020).

The multiphase model is appropriate when the population of (micro-) particles such as urine precipitation or stone fragments becomes significant. The solution procedure usually starts with solving the velocity field, and then to use the result in the Basset–Boussinesq–Oseen (BBO) equation for particles with small Stokes numbers (Jiménez-Lozano, 2009, Jiménez-Lozano et al., 2011, Jiménez-Lozano & Sen, 2010, Rath & Reese, 1984, Riaz & Sadiq, 2020). The BBO equation for the motion of a particle can be written as the sum of forces acting on it, that is, the Stoke's drag, the pressure force, the virtual mass (due to the inertia of accelerating or decelerating particles), the Basset force (due to the relative acceleration between particles with respect to the fluid), and the body force (e.g., gravity). With the initial conditions of particle position and velocity, the BBO equation can be solved numerically to obtain the particle position in time. As such, independent particle trajectories can be solved, and the dispersion of particles can be analyzed under different flow conditions.

In a two-dimensional ureter model with infinite sinusoidal waves and different contraction level, the resulting particle trajectory reveals a positive correlation between contraction level and particle transportation. The efficacy of particle trapping (due to the recirculation of local streamlines) is shown to increase with the amplitude ratio ϕ of the peristaltic wave, defined as the wave amplitude over the ureter radius such that $\phi = 0$ corresponds to a constant-area tube, while $\phi = 1$ describes a completely occluded tube (Jiménez-Lozano, 2009; Jiménez-Lozano & Sen, 2010). Following that, Jiménez-Lozano et al. (2011) implemented a model assuming an axisymmetric tube containing an incompressible, Newtonian fluid, in which identical, solid spheres are distributed. The number of trapped particles is shown to increase as the flow rate in the moving frame increases, which describes the difference between the wave propagation speed and the urinary flow velocity (Jiménez-Lozano et al., 2011). These results may be used to simulate the aggregation and sedimentation of crystalline particles, bacteria, or stone fragments in the urinary tract, which are important processes involved in encrustation and biofilm formation on urological devices.

Finally, there exist a few studies to model urine as a non-Newtonian fluid, such that the viscosity is no longer constant under different stress levels (Hariharan et al., 2008; Rath & Reese, 1984). This assumption might be appropriate when considering pathological changes to the urine such as haematuria and bacteriuria, although experimental validation of urine viscosity under pathological conditions might be needed to fully justify the use of these models.

4 | COMPUTATIONAL METHODS

4.1 | Computational fluid dynamics models

One of the advantages of computational fluid dynamics (CFD) models is the convenience to simulate multiple configurations by systematically varying the model parameters, allowing for more comprehensive analyses in a cost/time efficient manner. There are several commercially available CFD packages, for example, ANSYS (Ansys Inc., PA) and COMSOL Multiphysics (Comsol Inc., Stockholm, SE), or open source software, for example, OpenFOAM, with considerable amount of tutorials and examples for general introductions on their implementation.

In CFD models, the ureter is often modeled as a solid tube with various shapes (Figure 3(a)–(d)), and the flow regime within an identified computational domain is solved. They are mostly used to study the design parameters and configurations of ureteral stents for the convenience mentioned above. Tong et al. (2006) published probably the first CFD study of the stented ureter, where the intraluminal and extraluminal urine flow were evaluated for several side hole configurations, such as number of side holes (0, 11, and 17), their angular position, and inner diameter. They also introduced partial blockages either internal or external to the stent, and showed that only the side holes immediately upstream and downstream of local blockages were active (i.e., they exchanged intraluminal and extraluminal flows). Additionally, Tong et al. (2006) claims that the majority of side holes serve no clear function in the absence of blockages.

To further study the effect of local obstructions, Carugo et al. (2014) and Clavica et al. (2014) computed the 2D laminar flow field of an obstructed ureteral stent, as illustrated in Figure 3(e). This model was used to study the flow in the vicinity of a side hole, especially in the small cavity between a complete obstruction and the first downstream side hole. It was hypothesized that low-velocity cavity flow may cause entrapment of particulate bodies (i.e., encrustation crystals or bacterial cells). The BCs in this study were defined as follows: stent and ureter walls were stationary, and no slip condition was applied on all surfaces; urine flowed into the stent upstream of the obstruction and was the only source of incoming fluid; and the outlet pressure was fixed at 0 Pa, meaning that no bladder activity was incorporated. The results suggest that the number of laminar vortices forming in the cavity increases with larger gap size D and smaller

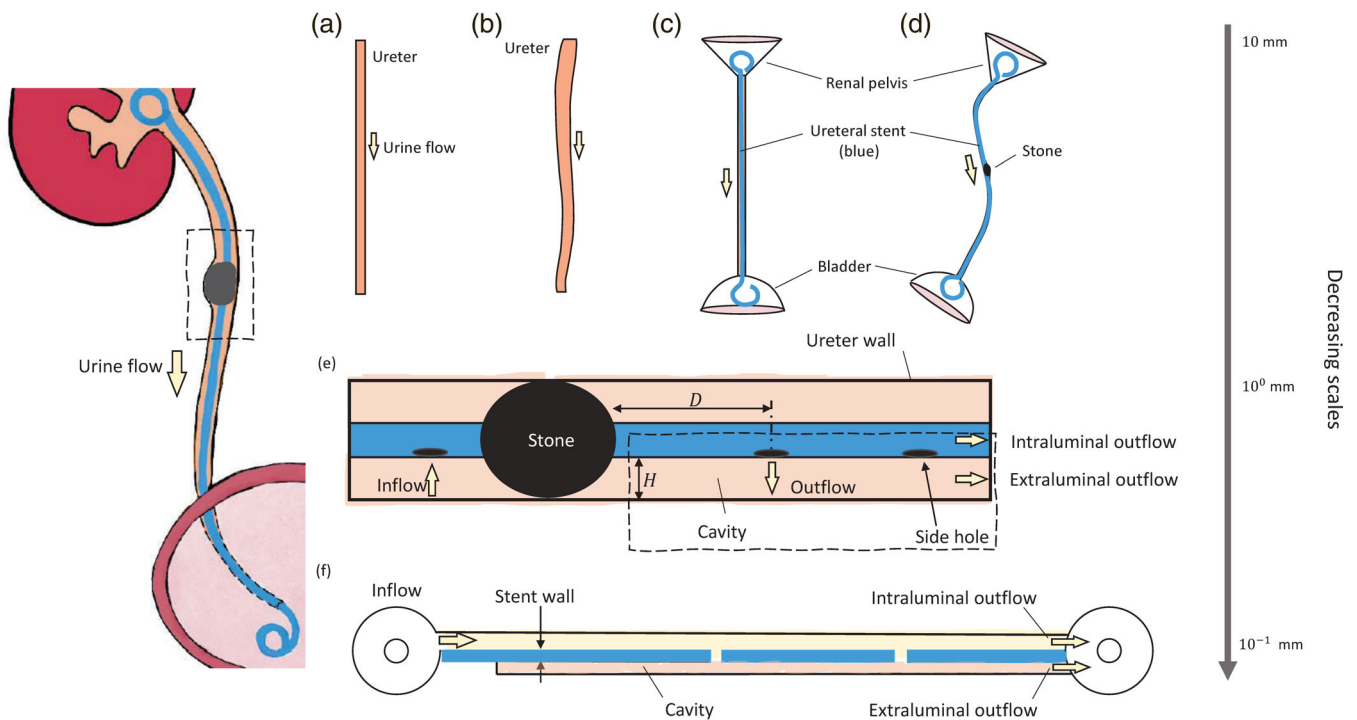


FIGURE 3 Illustration of a common computational setup for the UUT at different scales from 10 mm to 10^{-1} mm. A general layout of the UUT is shown on the left for reference, where the indwelling stent and urinary stones are also illustrated. (a)–(d) Various geometries for computational ureter models. The ureter can be modeled as straight, curved, tapered, or undulated tubes (a,b). An unstented ureter is often used to study the peristalsis of the ureter and the interaction between urine boluses and ureter walls. Renal pelvis and bladder are sometimes included at boundaries to prescribe the pressure conditions (c,d). In all cases, stent models can be included to evaluate the efficacy of different design parameters such as stent diameters, number of side holes, and so on. (e) Computational domain (marked by dashed rectangle on the left) to study urine flow through the stented ureter in the presence of a stone. In this scenario, the upstream urine flow is forced to enter the side hole and partially exits to create both intraluminal and extraluminal flows. A cavity in the downstream vicinity of the stone is created, influenced by the distance (D) between the stone and the first downstream side hole and the height (H) of the extraluminal space. (f) Computational domain on a smaller scale (marked by dashed rectangle in (e)) to study detailed architecture of the stent such as wall thickness, side hole diameter and vertex angle, and so on

extraluminal space H , as defined in Figure 3(e), leading to increased risk of developing encrustation. This conclusion suggests a higher rate of encrustation in the downstream vicinity of obstructions, such that the axial location of side holes relative to the obstruction could be of clinical interests.

Simulations of urine flow in stented ureters with different configurations in terms of ureter geometry, stent architecture, and local stenosis have been carried out extensively over the past few years (Kim et al., 2015a, 2015b; Kim et al., 2017a, 2017b; Kim, Kim, Choi, Lee, Baba, & Suh, 2020). Notably, the geometry of the curved ureter (Figure 3(d)) adopted by Kim et al. (2015b) is reconstructed from real human ureters, using computed tomography (CT) images of the UUT from 19 healthy males. The renal pelvis and bladder are modeled by two conical chambers at each end (Figure 3(c), (d)). Their results, in contradiction to the previous conclusion from Tong et al. (2006), suggest that the side holes are active even without stenosis, and a larger number of side holes even increases the total flow rate, although to a very limited extent. The flow exchange through these side holes seems to be more effective in the curved ureter models than in the straight ones.

In consecutive studies more configurations of the stent/ureter model are studied to understand the effect of side holes and the ureter diameter (Kim et al., 2015a; Kim et al., 2017a, 2017b; Kim, Kim, Choi, Lee, Baba, & Suh, 2020). In the work of Kim et al. (2017a), 20 cases are studied with different levels of ureteral stenosis (33, 52, 74, and 88% blockage based on cross sectional area) and with several side hole configurations. It is shown that side holes around the stenosis increase the total flow rate, in agreement with Tong et al. (2006), and that this enhancement increases with higher degree of stenosis blockage. Effects of the overall ureter shape, that is, tubular, funnel-shaped, and undulated are also studied by Kim et al. (2017b) and Kim, Choi, Lee, Baba, and Suh (2020), and the authors concluded that the

ureter shape closest to the human ureter (such as that from a CT scan) should be always considered first to obtain more accurate results.

Recently, Mosayyebi et al. (2019) and De Grazia et al. (2020) conducted CFD simulations on stent-on-chip (SOC) models to understand the microscopic wall shear stress (WSS) distribution in proximity to a urinary obstruction. One computational setup is illustrated in Figure 3(f), and the dimensions of the microfluidic device are similar to those of a stented ureter. The study is focused on local geometry changes of stents, such as the shape of the side holes and the thickness of stent walls. Their computational result, combined with experimental results, show an inverse correlation between the magnitude of WSS and the deposition rate of encrusting particles, and a positive correlation between bacterial coverage area and number of cavities in the flow. The authors managed to manipulate the magnitude of WSS by optimizing the stent wall thickness, streamlining the side hole cross sectional shape, and by including multiple side holes in the vicinity of the obstruction (De Grazia et al., 2020; Mosayyebi et al., 2019).

4.2 | Fluid–structure interaction models

Fluid–structure interaction (FSI) models, as indicated by the name, are often implemented to explore the interactions between the fluid and the solid components of the UUT. They differ from CFD models by modeling the structural behavior of solid surfaces with constitutive equations instead of rigid boundaries. Several computational packages can be used with FSI solvers, such as ANSYS (Ansys Inc., PA) or ADINA (ADINA R & D, Inc., MA).

The earliest available FSI study of the urinary system is given by Vahidi and Fatouraee (2007) and Vahidi et al. (2011), where peristalsis of the ureter is revisited after the reduced order models previously proposed. In this context, the fluid domain is governed by the incompressible Navier–Stokes equations, and the solid part (denoted by the superscript s), that is, ureter wall, is modeled as a linear elastic material such that

$$\rho^s \frac{\partial^2 \mathbf{d}^s}{\partial t^2} - \nabla \cdot \boldsymbol{\sigma} = \mathbf{B}, \quad (14)$$

where ρ^s is the solid density, \mathbf{d}^s is the solid displacement, $\boldsymbol{\sigma}$ is the Cauchy stress tensor, and \mathbf{B} is the body force. Note that, the displacement of the solid as a result of its interaction with fluid is solved here, whereas in peristalsis models presented before the motion of the wall is prescribed.

In terms of the material properties of the ureter wall, Rassoli et al. (2014), Sokolis et al. (2017), Sokolis (2019, 2020) are among the few who provided studies on the strain–stress properties of human ureters. In a complementary approach, Toro and Siviglia (2013) formulated a one-dimensional time-dependent nonlinear mathematical model for collapsible tubes with discontinuous mechanical properties. These works might be useful for case studies to model pathologically affected ureters, where wall thickness, Young's modulus and cross sectional area can be discontinuous.

At the interface of the fluid–solid (F–S) domain (denoted by the superscript f and s , respectively), the no-slip condition is imposed (Vahidi et al., 2011; Vahidi & Fatouraee, 2007), where the displacement and velocity on the F–S interface, respectively, remain such that

$$\begin{aligned} \mathbf{d}^f &= \mathbf{d}^s, \\ \partial \mathbf{d}^f / \partial t &= \partial \mathbf{d}^s / \partial t. \end{aligned} \quad (15)$$

The dynamic coupling condition is given by continuity of normal and tangential stress:

$$\mathbf{n} \cdot \boldsymbol{\sigma}^f = \mathbf{n} \cdot \boldsymbol{\sigma}^s, \quad (16)$$

where \mathbf{n} is the unit vector normal to the interface. The solution was obtained using the arbitrary Lagrangian–Eulerian formulation (Hirt et al., 1974), which allows the mesh to move arbitrarily to precisely track the deformation of the interface between the fluid domain (Eulerian) and the solid domain (Lagrangian). Further discussions on the solution method can be found in Benra et al. (2011). It was shown that the flow rate increased almost linearly with the height of

the peristaltic wave (i.e., the level of ureter wall contraction), and retrograde reflux of urine at the start of the contraction was observed.

In a consecutive study, Vahidi and Fatourae (2012) incorporated in-vivo morphometric data of the ureteral lumen during peristalsis. The ureter is modeled as an axisymmetric tube with a urine bolus traveling inside due to peristalsis. In contrast to the study by Vahidi et al. (2011), the ureteral wall was modeled as an hyperelastic material using the Arruda-Boyce model (Arruda & Boyce, 1993). The ureter wall was fixed at both ends as a BC for the solid domain. Their results showed a smaller flow rate compared to previous reported values due to the back flow of urine into the kidney.

Takaddus and Chandy (2018) presented the first full three-dimensional FSI model on obstructed ureters with peristaltic waves. The ureter is modeled as a 30 cm long tube with its two ends fixed, and the stone is modeled as a fixed spherical obstruction of varying size. The wall is modeled based on ex-vivo experimental data from Rassoli et al. (2014), assuming a nearly incompressible material. The peristalsis is considered to be a Gaussian pulse of expansion forces creating a deformation of length 10 mm and 1 mm in diameter, with a maximum pressure value of 2.1×10^5 Pa traveling at 2 cm/s toward the outlet of the ureter. The results, interestingly, suggested that both shear stress and pressure distribution profiles (two of the most important parameters to quantify the effect of an obstruction) are similar to a 2D simulation of the same problem assuming axisymmetry (Takaddus et al., 2018), which is computationally cheaper.

To include further components of the urinary system, one may also prescribe a BC to include the functionality of UVJ, which acts like a valve to close the ureter during the voiding phase and prevent reflux (Juskiewenski et al., 1984). Villanueva et al. (2015, 2018) studied the UVJ competence, where the ureter wall is modeled as a viscoelastic material after Yin and Fung (1971). The pressures needed to collapse the ureter tube with different diameter, wall thickness, and length are studied. A volcano-type of UVJ connection, where the ureter is surrounded by mucosa at the ureteral orifice (forming a volcano-like surface), is shown to require 78% less closing pressure than that for the golf-type orifice (flush surface), and that the intravesical length of the ureter does not affect the closing pressure.

Finally, Gómez-Blanco et al. (2016) designed a study to justify the need of FSI methods in urinary flow simulations in comparison with CFD models. In that study, the ureteral wall is modeled as an isotropic hyperelastic quasi-incompressible material. Experimental data of stress-strain curves found in the literature are used to fit the material models tested in the study, that is, neo-Hookean, Mooney-Rivlin, Yeoh, and one-term Ogden model (Gómez-Blanco et al., 2016). The parameters in each model are fitted in the axial direction using published ex-vivo test data (Rassoli et al., 2014). The F-S interface is treated using Equations (15) and (16). Their results, however, suggest that the stented ureter with urine flow behaves nearly as a rigid body, and could be replaced by a simple CFD simulation, at least for the test conditions reported therein. Even though the assumptions of the ureter model is arguable, that is, isotropy and quasi-incompressibility, this conclusion calls for further investigations to evaluate the use of advanced numerical methods such as FSI.

5 | EXPERIMENTAL METHODS

To complement theoretical and computational models, in-vitro experiments of various kind have been carried out. These experimental models can be grouped into three categories: reactor models, where the purpose of study is focused on the chemical/biological aspects to understand biofilm formation and encrustation processes; flow models, where the fluid dynamics of the urine flow is probed; and microfluidic models, where small scale flow characteristics of order 0.1 mm are analyzed in relation to the behavior of microparticles. An overview of the components, considerations, and general solutions to the design and construction of experimental models of the urinary system is given in Figure 4.

5.1 | Reactor models

The reactor models, as defined above, focus on the biological/chemical aspects (such as bacterial growth with macro-scale analysis) of the urinary system. In this review, we omit the discussions on sample preparation and bacterial/chemical behaviors at micron and sub-micron scales. Instead, the focus is on the methodologies to simulate the UUT and the considerations/limitations associated with each model.

The earliest experiments focus mainly on the physiological functioning of the bladder, for example, volume capacity, residual volume and voiding frequency, to study the bulk bacterial growth (O'Grady & Pennington, 1966) and/or bacterial susceptibility to antibiotics (Greenwood & O'Grady, 1978). The bladder is often modeled as a static flask of

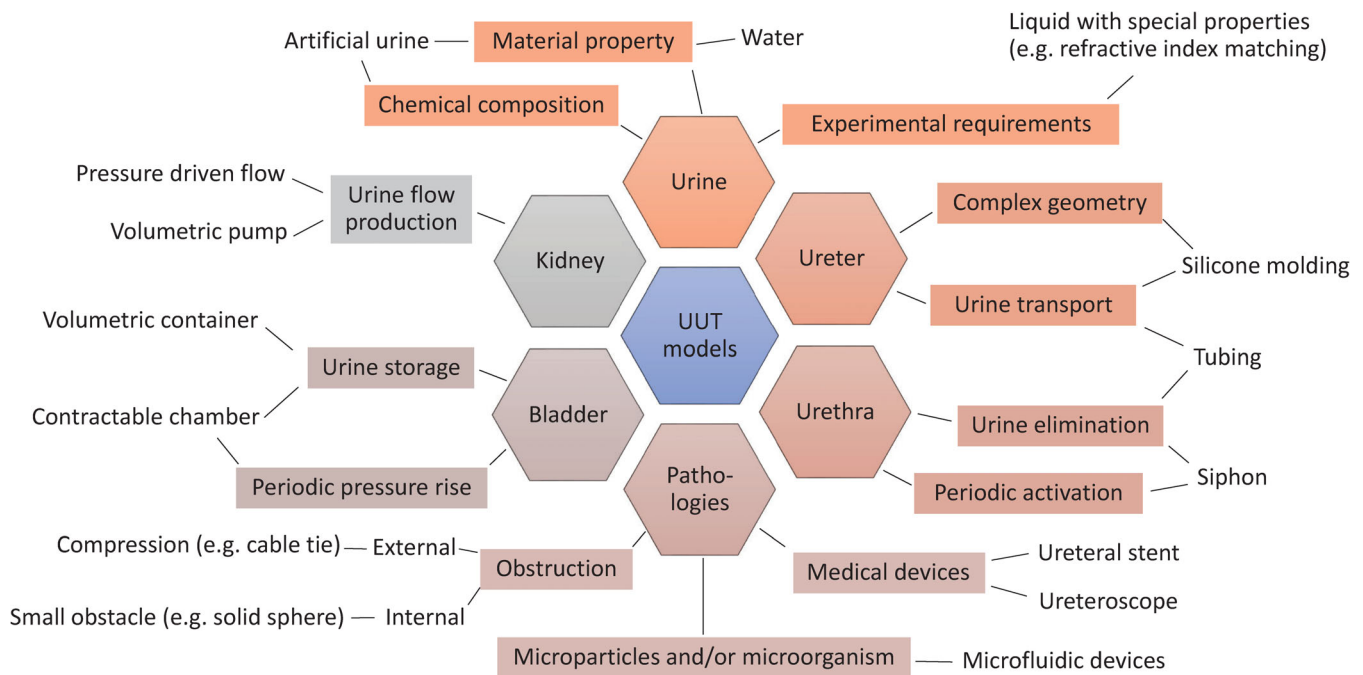


FIGURE 4 Modular diagram of the components (colored hexagons), considerations (colored rectangles), and general solutions (plain texts) summarized to inform the design process for an experimental model. For multi-organ models, concerns to connect each one of the component need to be addressed as well. Note that, in the context of the current discussion, pathological conditions primarily refer to obstructions, medical devices, microparticles, and/or microorganisms

about 400 ml in volume, with periodic voiding at predetermined time cycles (e.g., from every 100 min to 16 h) to simulate the micturition. Different values for postvoiding residual volume are also simulated by reserving 3–30 ml of urine in the bladder model. O’Grady and Pennington (1966) demonstrated that frequent micturition can reduce the amount of microbial organisms in the urinary tract. To model the functionality of the kidney, O’Grady and Pennington (1966) implemented a metering pump to simulate a urine production rate of 1 ml/min, whereas Greenwood and O’Grady (1978) included an “artificial kidney” (or gradient forming device, Mixo-Grad, Gilson Medical Electronics, WI) to simulate the renal excretion of antimicrobial agents. The gradient forming kidney model could be useful to study the synergy of antibiotics for the urinary system, or to prescribe the temporal condition of the chemical environment in the UUT.

To test the dynamics of microorganisms (or biofilm induced urinary stones) in a physiologically realistic scenario, the model proposed by Hobbs et al. (2018) is appropriate. The kidney and bladder analogues are made from the CDC Biofilm Reactor (BST Corp., MT), which comes with a stirring vane and eight suspended coupon holders attached to the lid, providing 24 disk-shaped coupons for periodic sampling of attached bacteria and precipitates. To simulate micturition periodically, the bladder analogue is emptied every four hours, leaving a residual volume of approximately 25 ml. Results from the model reveal the time-lagged retrograde ascension of microbes from the bladder into the kidney, which is impossible to capture using previous models.

With the invention of ureteral stents in the late 1960s, much attention has focused on understanding the interaction between microorganisms and stents. Various reactor models have been developed to investigate the stent’s susceptibility to biofilm development and encrustations. Regarding the fluid dynamics, both static and active models have been introduced. Static models usually incorporate a large reservoir or tank filled with AU, where the stent samples are submersed. One reactor model was designed by Tunney et al. (1996), consisting of a simple Perspex tank hosted in an incubator at 37°C. The tank is filled with AU and is constantly agitated by two magnetic stirrers. Multiple sections of stents were submersed in the AU and were removed at suitable time intervals to analyze the formed encrustations. Urease was included to mimic the effects of urea-splitting bacteria. Their results show a 60% surface coverage within 2 weeks and 100% by 10 weeks. Encrustations are mainly composed of hydroxyapatite and struvite, based on their analysis using infrared and X-ray diffraction spectroscopy. The obvious disadvantage of the static model is the lack of physiological functionalities such as micturition, which significantly influences the growth of chemicals and

microorganisms. To simulate the dynamics of physiological conditions, Choong et al. (2000) introduced the micturition cycle of the bladder by including a siphon at the bladder outlet, which empties the bladder chamber when the volume of urine reaches 300 ml. The volume can be changed by altering the height of the siphon. Other parts of the model consist of rigid glass parts representing a kidney, a ureter, and a bladder, connected in such a way to resemble the UUT. With this model, various stent materials can be tested for encrustation rates using artificial and human urine, respectively, in a physiologically-realistic environment. However, only one stent can be tested at a time, which limits the possibility of long term experiments with a large number of stent samples.

A possible solution to test multiple samples simultaneously is another type of model which incorporates only the ureter (e.g., simply a glass tube), and prescribes the urine flow rate using volumetric pumps (Cauda et al., 2017; Gorman et al., 2003; Hobbs et al., 2018). The model from Gorman et al. (2003) consists of a glass reaction vessel to represent the ureter, where three mandrels with stent samples on them are anchored in the rubber stoppers at each end. The inflow and outflow rates are at 10 ml/min, driven by a pump connected to an AU reservoir. The reaction vessels, pumping system and reservoir were all maintained at 37°C. This setup allows direct comparison of stent encrustation for different indwelling duration by keeping all other factors (e.g., geometry, flow rate, and pressure drop across the stent) constant during experiments, which helps to reduce random sources of error. Their results suggest that the encrustations under static conditions are significantly higher (in terms of mass, as measured by Atomic Absorption Spectrometry) than those under dynamic conditions, and therefore challenges the direct applicability of static reactor models. The same approach was also adopted by Cauda et al. (2017) for long-term quantification of encrustations (up to 6 months) on double-J stents, where the composition and amount of encrustations were analyzed using a Field Emission Scanning Electron Microscope. A drawback of this type of model is the steady flow circulation, where outflow rate is equivalent to the inflow rate due to the closed ureter model, without the periodic filling and voiding of bladder. As such, the actual growth rate of biofilm and encrustations might be different as the bladder activity will affect the bacterial growth too.

5.2 | Flow models

Some flow models focus mainly on the drainage capabilities to evaluate the performance of stent designs. As a consequence, the functionality of these in-vitro systems is largely simplified. For example, Hofmann and Hartung (1989) modeled the ureter as a 9-F (3 mm) polyvinyl tube with a stent inside, while a reservoir chamber at the top was used to model the kidney. To simulate urinary obstructions at different locations, three threads were tied around the tubing. The set-up therefore allows the evaluation of the intraluminal drainage capabilities of stents. Hofmann and Hartung (1989) also used an explanted cadaverous human urinary system to insert stents of various designs, and concluded that the ESWL (Extracorporeal SWL) stent with stellate cross section demonstrated the best drainage performance.

A similar model was also developed by Lange et al. (2011) to test drainage of specific stent designs. It consists of a silicone based cannula with wall thickness and elasticity similar to those of a porcine ureter, and a reservoir on top to mimic the kidney. A UltraCal30 (USG Corp., IL) casted sphere is inserted to mimic an obstruction. The head pressure is maintained by keeping a water column of 20 cm constant in the reservoir with a circulating pump. By comparing the total flow rates with different indwelling stents, it is shown that the drainage efficiency is affected by various design features of the stent, and is not solely correlated with the stent diameter.

To investigate the intraluminal flow of the stent, Olweny et al. (2000) designed a model without simulating the UUT, but directly connecting two stopcocks at each end of the nonfenestrated stent segment. Two glass columns of diameter 2.8 mm are then mounted to the vertical arm of the stopcocks, and the pressure difference is given by the water column height. The incoming flow rate is regulated by an infusion pump running at a constant flow rate from 2 to 10 ml/min, and the outflow is collected and measured at the outlet of the stent. The characteristic hydraulic resistance of each stent sample is calculated according to Poiseuille's law. However, their in-vitro results failed to agree with in-vivo data, which can be partially attributed to the morphological and functional changes of ureter (i.e., reduced or lost of peristalsis), associated with indwelling stents.

Most recently, Kim, Kim, Choi, Lee, and Baba (2020) proposed a UUT model with a pressure driven flow setup, consisting of two large square tanks (side length of 50 cm) containing fluids at different levels, and a ureter model connected in between. The ureter model is manufactured by molding silicone into a ureter mold resembling a real human ureter, based on measurements from CT scans. To start the experiment, the fluid levels at each tank are set to 20 cm (at the kidney side) and 4 cm (at the bladder side), respectively, and the resulting pressure difference drives the flow. The results on the total flow rate from different stents suggest an inverse correlation with the stent diameter, suggesting

higher resistance for stents with larger diameter. It is also shown that the curved and undulated ureter model demonstrates reduced flow rates compared to the straight model. Therefore, curved and undulated configurations (being more physiological) should be adopted for more meaningful and clinically relevant studies.

Toward more realistic physiological conditions, both ureteral peristalsis and body movement have been briefly attempted. Graw and Engelhardt (1986) designed perhaps the only experiment with reference to the ureteral peristalsis. The model ureter consists of 24 inflatable cuffs (air cushions) surrounding a thin-walled inner tube with four lobes resembling a cross-like shape. The inner tube can be dilated as bolus of fluid (or a catheter) enters, and the cuffs can be inflated for a total occlusion of the inner tube. As such, the peristaltic wave, and consequently bolus of fluid, can be produced by periodically adjusting the pressure levels in each cuff. From the pressure measurements, both intraluminal and maximum contraction pressure are shown increase with larger catheter diameters, and it is recommended that the maximum catheter size should not exceed the half-width of the lumen, with reference to the uromanometrogram in urological practice.

To simulate the respiratory and skeletal movement, Stoller et al. (2000) designed a mechanical urinary model, which is the only study to date addressing the effect of body movement on the flow rate within stented ureters. The movement between stent and the surrounding ureter wall is introduced by oscillating the stent through a prescribed excursion distance of 1 cm along the axial direction. The renal pelvis is simulated with a funnel with a constant water level. The ureter is modeled by several rigid tubes with varying internal diameters. Water passing through and/or around the stent is collected over a certain period of time. To differentiate between the intraluminal and extraluminal flows, a guide wire was used to obstruct the stent lumen to measure the extraluminal flow volume. Their results show that spiral-ridged double-J stents provide the greatest flow rate, and that the axial movement increases drainage of the spiral-ridged stents. From a fluid mechanical perspective, the results are not surprising as the axial movement imposes a pressure gradient due to the spiral ridge on the stent surface.

In terms of bladder movement, the expansion/collapse of the bladder wall with increasing/decreasing internal volume is also important but rarely incorporated. The model proposed by Kim et al. (2011) is of interest here. The bladder model, made in the form of a hemispherical capsule, incorporates an inner rubber membrane, and a gap between the membrane and the external capsule. The rubber membrane can be filled up to a specific volume between 100 and 600 ml, and air can be injected into the hemispherical gap using a syringe pump to replicate the abdominal pressure. This special configuration allows simulations of physiological volume-pressure curves, which might be used for patient specific models. Micturition is also realized by opening the outlet valve when the target peak bladder pressure is reached. Four pressure transducers were installed at the inlet (ureter) and outlet (urethra) hoses of the bladder model, and at 1/3 and 2/3 height within the bladder capsule, respectively, to monitor the pressure difference in the bladder. The peak bladder pressure during micturition is measured between 20 and 80 cmH₂O, which is within the physiological range.

In addition to studies evaluating the overall performance of stents, growing interest on the mechanism of development of biofilm and encrustations has also sparked experimental models at smaller scales. Carugo et al. (2013) and Clavica et al. (2014) designed an in-vitro transparent model based on porcine ureter characteristics. The ureter model incorporates a small cylindrical chamber (20 mm in diameter and 36 mm in height) as the renal pelvis proximal to the ureter. The actual ureter model is further divided into upper, middle, and lower segments with varying diameters based on ex-vivo measurements from eight pig ureters. Furthermore, they modeled different obstructions using plastic spheres to create different blockage ratios in the cross sectional area. Inlet pressure is recorded using a transducer placed in the renal pelvis chamber, and the outlet of the ureter is maintained at atmospheric pressure. The flow is driven by a syringe pump at constant rate. The working fluid is a solution of glycerol and deionized water. Five different viscosities are realized to mimic different urine characteristics, that is, caused by pathological changes. The results established a relation between the fluid viscosity, flow rate, and the renal pressure, showing that a small increase in the obstructed area will significantly increase the renal pressure for a given viscosity and flow rate. Notably, these studies (Carugo et al., 2013; Clavica et al., 2014) are the first to perform flow visualization experiments inside a transparent ureter model using fluorescent particles. Microscopic images revealed laminar vortices in the cavity downstream of the obstruction (similar to that in Figure 3(e)). Possible relations between these laminar vortices and encrustation are discussed, and it is hypothesized that laminar vortices may act as anchoring sites for encrusting deposits and bacteria.

5.3 | Microfluidic models

To examine smaller scale features, microfluidic “SOC” models (i.e., experimental counterparts of the computational models shown in Figure 3(f)), have been developed by Mosayyebi, Yue, et al. (2018) using a microchip to study the hydrodynamics of stent-ureter interactions. In general, the polydimethylsiloxane chip incorporates a large and a narrow channel, representing the intra- and extraluminal compartments of a stented ureter, respectively. The two compartments are separated by a 0.5 mm thick wall (stent wall thickness). Obstructions in the ureter are represented by a cavity upstream of two side holes (Figure 3(f)). The flow is driven by a peristaltic pump, circulating supersaturated AU at flow rates of 1 and 10 ml/min. Fluorescent tracer particles of 5.6 μm mean diameter are suspended in the fluid, and the circulation is maintained for 90 min for each experiment. Microscope images are then taken to observe encrusting precipitations from the AU near the cavity and side holes. By comparing to the numerical results, an inverse correlation between WSS magnitude and particle accumulation is revealed. In the consecutive study by Mosayyebi et al. (2019), the same model was used to investigate the effects of varying stent thickness and side-hole shapes, and a novel streamlined side-hole architecture was proposed that led to a significant reduction in the amount of particle deposition.

To further study the bacterial attachment in ureteral stents, the SOC devices from (Mosayyebi et al., 2019; Mosayyebi, Yue, et al., 2018) are modified by De Grazia et al. (2020) to simulate more complex obstructions of the stented ureter. The ureter is modeled as a 5 mm wide channel, and side holes are included as openings between the intra- and extraluminal channels. The bacterial coverage area was found to be directly proportional to the number of cavities in the model, which were associated with low WSS levels. Finally, the fluid mechanical characteristics are deemed as key factors for a novel technology solution against bacterial attachments.

6 | CONCLUDING REMARKS

Judging from the increasing number of publications on the subject over the past ten years, a resurgence of fluid mechanical studies of the UUT is evident. Table A1 gives an overview of previous studies of the urinary tract using different modeling methods, focusing on various physiological and pathological conditions at various scales. The table reveals the gaps in the development of methodologies and models in the study of UUT. Reduced order methods exploit the disparate length scales inherent in the system to obtain results that retain the key dominant physics, but they are less directly clinically applicable in terms of specific geometrical features, and therefore complement full computational models. Computational models are more capable to capture physiologically realistic anatomy, and to simulate fully 3D and time dependent dynamics, but the setup requires a series of assumptions and simplifications, which need to be carefully examined and justified. Experimental models, consequently, provide an excellent counterpart to reduced and computational models by providing physical tests under various physiological and pathological conditions. However, a faithful experimental replication of the physiological mechanics of the UUT may require systems of greater technological complexity (and potentially cost) than the ones reported so far.

For any modeling methodology, it is always helpful to use clinical references to establish the appropriate assumptions and physiologically meaningful parameters in order to have clinically relevant results, as detailed in Section 2. The availability of reduced-order models, computational tools, and experimental platforms means that a synergistic approach to UUT studies is possible through collective efforts. As such, a consensus between researchers and clinicians appears necessary to establish a mutual understanding of the most pressing issues in modern urological practice, directing the forthcoming research studies from a practical perspective.

The multiphysics and multiscale nature of the urinary system also inspires the utilization of tools and methodologies from several other research fields. For instance, biodegradable stents have drawn much attention in recent years, but no computational or experimental studies have demonstrated their performance against biofilm and encrustation over clinically relevant time scales. Such studies, together with recent advances in 4D printing (Sydney Gladman et al., 2016), may enable optimization of the design of ureteral stents by prescribing desired properties. Meanwhile, several studies in microbiology have shown the influence of fluid mechanical characteristics on microbial behavior (Kim, Olympiou, McCoy, Irwin, & Rimer, 2020; Laffite et al., 2016; Salta et al., 2013; Zalewska-Piatek et al., 2020) especially the correlation between the micro-scale shear stress field and the mobility or attachment of bacteria (Rusconi & Stocker, 2015; Sherman et al., 2019). These efforts will open new avenues to the study of urinary flows, leading to novel ideas and solutions for various urological symptoms, ultimately contributing to the well-being of individual patients.

ACKNOWLEDGMENTS

This work was supported by the Swiss National Science Foundation (SNSF grant number IZCOZ0_182966) and the European Cooperation in Science and Technology (ENIUS COST action, grant number CA16217).

CONFLICT OF INTEREST

The authors have declared no conflicts of interest for this article.

AUTHOR CONTRIBUTIONS

Shaokai Zheng: Writing-original draft. **Dario Carugo:** Writing-review and editing. **Ali Mosayyebi:** Writing-review and editing. **Ben Turney:** Writing-review and editing. **Fiona Burkhard:** Writing-review and editing. **Dirk Lange:** Writing-review and editing. **Dominik Obrist:** Writing-review and editing. **Sarah Waters:** Writing-review and editing. **Francesco Clavica:** Writing-review and editing.

ORCID

Sarah Waters  <https://orcid.org/0000-0001-5285-0523>

RELATED WIREs ARTICLES

[Lower urinary tract development and disease](#)

[Recent advances in computational methodology for simulation of mechanical circulatory assist devices](#)

[Measurement and modeling of coronary blood flow](#)

REFERENCES

- Alloussi, S. H., Lang, C., Eichel, R., Ziegler, M., Stenzl, A., & Alloussi, S. (2010). 692 urodynamical benchmarks: A retrospective analyses of 976 combined urodynamics with no pathological findings to evaluate standard values. *European Urology Supplements*, *9*(2), 227. [https://doi.org/10.1016/S1569-9056\(10\)60679-3](https://doi.org/10.1016/S1569-9056(10)60679-3)
- Arkusz, K., Pasik, K., Halinski, A., & Halinski, A. (2020). Surface analysis of ureteral stent before and after implantation in the bodies of child patients. *Urolithiasis*, *49*, 83–92. <https://doi.org/10.1007/s00240-020-01211-9>
- Arruda, E. M., & Boyce, M. C. (1993). A three-dimensional constitutive model for the large stretch behavior of rubber elastic materials. *Journal of the Mechanics and Physics of Solids*, *41*(2), 389–412. [https://doi.org/10.1016/0022-5096\(93\)90013-6](https://doi.org/10.1016/0022-5096(93)90013-6)
- Barros, A. A., Oliveira, C., Reis, R. L., Lima, E., & Duarte, A. R. C. (2015). Ketoprofen-eluting biodegradable ureteral stents by Co2 impregnation: In vitro study. *International Journal of Pharmaceutics*, *495*(2), 651–659. <https://doi.org/10.1016/j.ijpharm.2015.08.040>
- Barros, A. A., Oliveira, C., Ribeiro, A. J., Autorino, R., Reis, R. L., Duarte, A. R. C., & Lima, E. (2018). In vivo assessment of a novel biodegradable ureteral stent. *World Journal of Urology*, *36*(2), 277–283. <https://doi.org/10.1007/s00345-017-2124-3>
- Benra, F.-K., Dohmen, H. J., Pei, J., Schuster, S., & Wan, B. (2011). A comparison of one-way and two-way coupling methods for numerical analysis of fluid-structure interactions. *Journal of Applied Mathematics*, *16*, 2011. <https://doi.org/10.1155/2011/853560>
- Bevan, T., Carriveau, R., Goneau, L., Cadieux, P., & Razvi, H. (2012). Numerical simulation of peristaltic urine flow in a stented ureter. *American Journal of Biomedical Science*, *4*(3), 233–248.
- Birch, B. R. P., Das, G., & Wickham, J. E. A. (1988). Tethered ureteric stents—A clinical assessment. *British Journal of Urology*, *62*(5), 409–411. <https://doi.org/10.1111/j.1464-410X.1988.tb04385.x>
- Bykova, A. A., & Regirer, S. A. (2005). Mathematical models in urinary system mechanics. *Fluid Dynamics*, *40*(1), 1–19. <https://doi.org/10.1007/s10697-005-0039-y>
- Carew, E. O., & Pedley, T. J. (1997). An active membrane model for peristaltic pumping: Part i-periodic activation waves in an infinite tube. *Journal of Biomechanical Engineering*, *119*(1), 66–76. <https://doi.org/10.1115/1.2796066>
- Carugo, D., Elmahdy, M., Zhao, X., Drake, M., Zhang, X., & Clavica, F. (2013). An artificial model for studying fluid dynamics in the obstructed and stented ureter. In *35th Annual International Conference of the IEEE Engineering in Medicine and Biology Society (EMBC)*, IEEE, pages 5335–5338.
- Carugo, D., Zhang, X., Drake, J. M., & Clavica, F. (2014). Formation and characteristics of laminar vortices in microscale environments within an obstructed and stented ureter: A computational study. In *Proceedings of the 18th International Conference on Miniaturized Systems for Chemistry and Life Sciences, MicroTAS*. The Chemical and Biological Microsystems Society.
- Cauda, V., Chiodoni, A., Laurenti, M., Canavese, G., & Tommasi, T. (2017). Ureteral double-j stents performances toward encrustation after long-term indwelling in a dynamic in vitro model. *Journal of Biomedical Materials Research*, *105*(8), 2244–2253. <https://doi.org/10.1002/jbm.b.33756>
- Chen, X., Summers, R. M., & Yao, J. (2013). Kidney tumor growth prediction by coupling reaction-diffusion and biomechanical model. *IEEE Transactions on Biomedical Engineering*, *60*(1), 169–173. <https://doi.org/10.1109/TBME.2012.2222027>
- Chitty, L. S., & Altman, D. G. (2003). Charts of fetal size: Kidney and renal pelvis measurements. *Prenatal Diagnosis*, *23*(11), 891–897. <https://doi.org/10.1002/pd.693>

- Choong, S. K. S., Wood, S., & Whitfield, H. N. (2000). A model to quantify encrustation on ureteric stents, urethral catheters and polymers intended for urological use. *BJU International*, 86(4), 414–421. <https://doi.org/10.1046/j.1464-410X.2000.00861.x>
- Chrispell, J., & Fauci, L. (2011). Peristaltic pumping of solid particles immersed in a viscoelastic fluid. *Mathematical Modelling of Natural Phenomena*, 6(5), 67–83. <https://doi.org/10.1051/mmnp/20116504>
- Chua, R. Y. R., Lim, K., Leong, S. S. J., Tambyah, P. A., & Ho, B. (2017). An in-vitro urinary catheterization model that approximates clinical conditions for evaluation of innovations to prevent catheter-associated urinary tract infections. *Journal of Hospital Infection*, 97(1), 66–73. <https://doi.org/10.1016/j.jhin.2017.05.006>
- Clavica, F., Zhao, X., ElMahdy, M., Drake, M. J., Zhang, X., & Carugo, D. (2014). Investigating the flow dynamics in the obstructed and stented ureter by means of a biomimetic artificial model. *PLoS One*, 9(2), e87433.
- Cormio, L., Koivusalo, A., Makisalo, H., Wolff, H., & Ruutu, M. (1994). The effects of various indwelling jj stents on renal pelvic pressure and renal parenchymal thickness in the pig. *British Journal of Urology*, 74(4), 440–443. <https://doi.org/10.1111/j.1464-410X.1994.tb00419.x>
- Cummings, L. J., Waters, S. L., Wattis, J. A. D., & Graham, S. J. (2004). The effect of ureteric stents on urine flow: Reflux. *Journal of Mathematical Biology*, 49(1), 56–82.
- De Grazia, A., LuTheryn, G., Meghdadi, A., Mosayyebi, A., Espinosa-Ortiz, J. E., Gerlach, R., & Carugo, D. (2020). A microfluidic-based investigation of bacterial attachment in ureteral stents. *Micromachines*, 11(4), 408–421. <https://doi.org/10.3390/mi11040408>
- De Keulenaer, B. L., De Waele, J. J., Powell, B., & Malbrain, M. L. N. G. (2009). What is normal intra-abdominal pressure and how is it affected by positioning, body mass and positive end-expiratory pressure? *Intensive Care Medicine*, 35(6), 969–976. <https://doi.org/10.1007/s00134-009-1445-0>
- Diokno Ananias, C., Wells Thelma, J., & Brink Carol, A. (1987). Comparison of self-reported voided volume with cystometric bladder capacity. *Journal of Urology*, 137(4), 698–700. [https://doi.org/10.1016/S0022-5347\(17\)44179-6](https://doi.org/10.1016/S0022-5347(17)44179-6)
- Donahue, R. P., Stamm, A. W., Gibbons, R. P., Porter, C. R., Kobashi, K. C., Corman, J. M., & Lee, U. J. (2018). Evolution of the ureteral stent: The pivotal role of the gibbons ureteral catheter. *Urology*, 115, 3–7. <https://doi.org/10.1016/j.urology.2018.02.007>
- Edmond, P., Ross James, A., & Kirkland Ian, S. (1970). Human ureteral peristalsis. *Journal of Urology*, 104(5), 670–674. [https://doi.org/10.1016/S0022-5347\(17\)61808-1](https://doi.org/10.1016/S0022-5347(17)61808-1)
- Elbadawi, A. (1996). Functional anatomy of the organs of micturition. *Urologic Clinics of North America*, 23(2), 177–210. [https://doi.org/10.1016/S0094-0143\(05\)70304-9](https://doi.org/10.1016/S0094-0143(05)70304-9)
- Emamian, S. A., Nielsen, M. B., Pedersen, J. F., & Ytte, L. (1993). Sonographic evaluation of renal appearance in 665 adult volunteers: Correlation with age and obesity. *Acta Radiologica*, 34(5), 482–485. <https://doi.org/10.1177/028418519303400511>
- Fowler, C. J., Griffiths, D., & de Groat, W. C. (2008). The neural control of micturition. *Nature Reviews. Neuroscience*, 9(6), 453–466. <https://doi.org/10.1038/nrn2401>
- Fung, Y. C. (1967). Elasticity of soft tissues in simple elongation. *American Journal of Physiology-Legacy Content*, 213(6), 1532–1544. <https://doi.org/10.1152/ajplegacy.1967.213.6.1532>
- Gómez-Blanco, J. C., Martínez-Reina, F. J., Cruz, D., Pagador, J. B., Sánchez-Margallo, F. M., & Soria, F. (2016). Fluid structural analysis of urine flow in a stented ureter. *Computational and Mathematical Methods in Medicine*, 2016, 5710798, 2016. <https://doi.org/10.1155/2016/5710798>
- Gorman, S. P., Garvin, C. P., Quigley, F., & Jones, D. S. (2003). Design and validation of a dynamic flow model simulating encrustation of biomaterials in the urinary tract. *The Journal of Pharmacy and Pharmacology*, 55(4), 461–468. <https://doi.org/10.1211/002235702856>
- Graw, M., & Engelhardt, H. (1986). Simulation of physiological ureteral peristalsis. *Urologia Internationalis*, 41(1), 1–8. <https://doi.org/10.1159/000281147>
- Greenwood, D., & O'Grady, F. (1978). An in vitro model of the urinary bladder. *The Journal of Antimicrobial Chemotherapy*, 4(2), 113–120.
- Griffiths, D. J. (1985). The pressure within a collapse tube, with special reference to urethral pressure. *Physics in Medicine and Biology*, 30(9), 951–963. <https://doi.org/10.1088/0031-9155/30/9/007>
- Griffiths, D. J. (1987). Dynamics of the upper urinary tract: I. Peristaltic flow through a distensible tube of limited length. *Physics in Medicine and Biology*, 32(7), 813–822. <https://doi.org/10.1088/0031-9155/32/7/002>
- Griffiths, D. J. (1989). Flow of urine through the ureter: A collapsible, muscular tube undergoing peristalsis. *Journal of Biomechanical Engineering*, 111(3), 206–211. <https://doi.org/10.1115/1.3168367>
- Griffiths, D. J., Constantinou, C. E., Mortensen, J., & Djurhuus, J. C. (1987). Dynamics of the upper urinary tract: II. The effect of variations of peristaltic frequency and bladder pressure on pyeloureteral pressure/flow relations. *Physics in Medicine and Biology*, 32(7), 823–833. <https://doi.org/10.1088/0031-9155/32/7/003>
- Haleblian, G., Kijvikai, K., de la Rosette, J., & Preminger, G. (2008). Ureteral stenting and urinary stone management: A systematic review. *The Journal of Urology*, 179(2), 424–430. <https://doi.org/10.1016/j.juro.2007.09.026>
- Hariharan, P., Seshadri, V., & Banerjee, R. K. (2008). Peristaltic transport of non-newtonian fluid in a diverging tube with different wave forms. *Mathematical and Computer Modelling*, 48(7), 998–1017. <https://doi.org/10.1016/j.mcm.2007.10.018>
- Hendlin, K., Korman, E., & Monga, M. (2012). New metallic ureteral stents: Improved tensile strength and resistance to extrinsic compression. *Journal of Endourology*, 26(3), 271–274. <https://doi.org/10.1089/end.2011.0332>
- Hickling, D. R., Sun, T. T., & Wu, X. R. (2015). Anatomy and physiology of the urinary tract: Relation to host defense and microbial infection. *Microbiology Spectrum*, 3(4), 1–17. <https://doi.org/10.1128/microbiolspec.UTI-0016-2012>

- Hirt, C. W., Amsden, A. A., & Cook, J. L. (1974). An arbitrary lagrangian-eulerian computing method for all flow speeds. *Journal of Computational Physics*, 14(3), 227–253. [https://doi.org/10.1016/0021-9991\(74\)90051-5](https://doi.org/10.1016/0021-9991(74)90051-5)
- Hobbs, T., Schultz, L. N., Lauchnor, E. G., Gerlach, R., & Lange, D. (2018). Evaluation of biofilm induced urinary infection stone formation in a novel laboratory model system. *The Journal of Urology*, 199(1), 178–185. <https://doi.org/10.1016/j.juro.2017.08.083>
- Hofmann, R., & Hartung, R. (1989). Ureteral stents—Materials and new forms. *World Journal of Urology*, 7(3), 154–157. <https://doi.org/10.1007/BF01637374>
- Inman, B. A., Etienne, W., Rubin, R., Owusu, R. A., Oliveira, T. R., Rodrigues, D. B., Maccarini, P. F., Stauffer, P. R., Mashal, A., & Dewhirst, M. W. (2013). The impact of temperature and urinary constituents on urine viscosity and its relevance to bladder hyperthermia treatment. *International Journal of Hyperthermia*, 29(3), 206–210. <https://doi.org/10.3109/02656736.2013.775355>
- Jiménez-Lozano, J. (2009). *Peristaltic flow with application to ureteral biomechanics*. Notre Dame University.
- Jiménez-Lozano, J., & Sen, M. (2010). Particle dispersion in two-dimensional peristaltic flow. *Physics of Fluids*, 22(4), 043303. <https://doi.org/10.1063/1.3366665>
- Jiménez-Lozano, J., Sen, M., & Corona, E. (2011). Analysis of peristaltic two-phase flow with application to ureteral biomechanics. *Acta Mechanica*, 219(1–2), 91–109. <https://doi.org/10.1007/s00707-010-0438-y>
- Juskiewenski, S., Vaysse, P., Moscovici, J., de Graeve, P., & Guitard, J. (1984). The ureterovesical junction. *Anatomia Clinica*, 5(4), 251–259. <https://doi.org/10.1007/BF01798748>
- Khandwekar, A. P., & Doble, M. (2011). Physicochemical characterisation and biological evaluation of polyvinylpyrrolidone-iodine engineered polyurethane (Tecoflex®). *Journal of Materials Science: Materials in Medicine*, 22(5), 1231–1246. <https://doi.org/10.1007/s10856-011-4285-8>
- Khoo, C. C., Abboudi, H., Cartwright, R., El-Husseiny, T., & Dasgupta, R. (2018). Metallic ureteric stents in malignant ureteric obstruction: A systematic review. *Urology*, 118, 12–20. <https://doi.org/10.1016/j.urology.2018.01.019>
- Kim, D., Olympiou, C., McCoy, C. P., Irwin, N. J., & Rimer, J. D. (2020). Time-resolved dynamics of struvite crystallization: Insights from the macroscopic to molecular scale. *Chemistry—A European Journal*, 26(16), 3555–3563. <https://doi.org/10.1002/chem.201904347>
- Kim, H. -H., Choi, Y. H., Lee, S. B., Baba, Y., Kim, K. -W., & Suh, S. -H. (2015a). Numerical analysis of the urine flow in a stented ureter with no peristalsis. *Bio-medical Materials and Engineering*, 26(s1), S215–S223.
- Kim, H. -H., Choi, Y. H., Lee, S. B., Baba, Y., Kim, K. -W., & Suh, S. -H. (2017a). Numerical analysis of urine flow through the side holes of a double j stent in a ureteral stenosis. *Technology and Health Care*, 25(S1), 63–72.
- Kim, J., Lee, M. K., & Choi, B. (2011). A study on the fluid mechanical urinary bladder simulator and reproduction of human urodynamics. *International Journal of Precision Engineering and Manufacturing*, 12(4), 679–685. <https://doi.org/10.1007/s12541-011-0088-6>
- Kim, K. W., Choi, Y. H., Lee, S. B., Baba, Y., Kim, H. H., & Suh, S. H. (2015b). Numerical analysis of the effect of side holes of a double j stent on flow rate and pattern. *Bio-medical Materials and Engineering*, 26, S319–S327. <https://doi.org/10.3233/BME-151319>
- Kim, K. W., Choi, Y. H., Lee, S. B., Baba, Y., Kim, H. H., & Suh, S. H. (2017b). Analysis of urine flow in three different ureter models. *Computational and Mathematical Methods in Medicine*, 2017, 1–11. <https://doi.org/10.1155/2017/5172641>
- Kim, K. -W., Kim, H. -H., Choi, Y. H., Lee, S. B., & Baba, Y. (2020). Urine flow analysis using double j stents of various sizes in in vitro ureter models. *International Journal for Numerical Methods in Biomedical Engineering*, 36, 1–12. <https://doi.org/10.1002/cnm.3294>
- Kim, K. -W., Kim, H. -H., Choi, Y. H., Lee, S. B., Baba, Y., & Suh, S. -H. (2020). Arrangement of side holes in a double j stent for high urine flow in a stented ureter. *Journal of Mechanical Science and Technology*, 34, 949–954. <https://doi.org/10.1007/s12206-020-0144-1>
- Kinn, A. C., & Lykkeskov-Andersen, H. (2002). Impact on ureteral peristalsis in a stented ureter. an experimental study in the pig. *Urological Research*, 30(4), 213–218. <https://doi.org/10.1007/s00240-002-0258-1>
- Knudsen, L., Gregersen, H., Eika, B., & Frøkiær, J. (1994). Elastic wall properties and collagen content in the ureter: An experimental study in pigs. *Neurourology and Urodynamics*, 13(5), 597–606. <https://doi.org/10.1002/nau.1930130515>
- Laffite, G., Leroy, C., Bonhomme, C., Bonhomme-Courty, L., Letavernier, E., Daudon, M., Frochot, V., Haymann, J. P., Rouzière, S., Lucas, I. T., Bazin, D., Babonneau, F., & Abou-Hassan, A. (2016). Calcium oxalate precipitation by diffusion using laminar microfluidics: Toward a biomimetic model of pathological microcalcifications. *Lab on a Chip*, 16(7), 1157–1160. <https://doi.org/10.1039/C6LC00197A>
- Lange, D., Hoag, N. A., Poh, B. K., & Chew, B. H. (2011). Drainage characteristics of the 3f microstent using a novel film occlusion anchoring mechanism. *Journal of Endourology*, 25(6), 1051–1056. <https://doi.org/10.1089/end.2010.0722>
- Lobo, M. L. P., Favorito, L. A., Abidu-Figueiredo, M., & Sampaio, F. J. B. (2011). Renal pelvic diameters in human fetuses: Anatomical reference for diagnosis of fetal hydronephrosis. *Urology*, 77(2), 452–457. <https://doi.org/10.1016/j.urology.2010.06.049>
- Lykoudis, P. S., & Roos, R. (1970). The fluid mechanics of the ureter from a lubrication theory point of view. *Journal of Fluid Mechanics*, 43(4), 661–674. <https://doi.org/10.1017/S0022112070002653>
- McCarthy, T. A. (1982). Validity of rectal pressure measurements as indication of intra-abdominal pressure changes during urodynamic evaluation. *Urology*, 20(6), 657–660. [https://doi.org/10.1016/0090-4295\(82\)90326-0](https://doi.org/10.1016/0090-4295(82)90326-0)
- Mesrobian, H. G. O. (2009). Bypass pyeloplasty: Description of a procedure and initial results. *Journal of Pediatric Urology*, 5(1), 34–36. <https://doi.org/10.1016/j.jpuro.2008.07.007>
- Mitra, T. K., & Prasad, S. N. (1973). On the influence of wall properties and poiseuille flow in peristalsis. *Journal of Biomechanics*, 6(6), 681–693. [https://doi.org/10.1016/0021-9290\(73\)90024-9](https://doi.org/10.1016/0021-9290(73)90024-9)
- Mosayyebi, A., Lange, D., Yann Yue, Q., Somani, B. K., Zhang, X., Manes, C., & Carugo, D. (2019). Reducing deposition of encrustation in ureteric stents by changing the stent architecture: A microfluidic-based investigation. *Biomicrofluidics*, 13(1), 014101. <https://doi.org/10.1063/1.5059370>

- Mosayyebi, A., Manes, C., Carugo, D., & Somani, B. K. (2018). Advances in ureteral stent design and materials. *Current Urology Reports*, 19(5), 35.
- Mosayyebi, A., Yue, Q. Y., Somani, B. K., Zhang, X., Manes, C., & Carugo, D. (2018). Particle accumulation in ureteral stents is governed by fluid dynamics: In vitro study using a “stent-on-chip” model. *Journal of Endourology*, 32(7), 639–646.
- Mosli Hisham, A., Farsi Hasan, M. A., Al-Zimaity Mohammed, F., Saleh Tarik, R., & Al-Zamzami Mokhtar, M. (1991). Vesicoureteral reflux in patients with double pigtail stents. *Journal of Urology*, 146(4), 966–969. [https://doi.org/10.1016/S0022-5347\(17\)37976-4](https://doi.org/10.1016/S0022-5347(17)37976-4)
- Najafi, Z., Gautam, P., Schwartz, B. F., Chandy, A. J., & Mahajan, A. M. (2016). Three-dimensional numerical simulations of peristaltic contractions in obstructed ureter flows. *Journal of Biomechanical Engineering*, 138(10), 1–7. <https://doi.org/10.1115/1.4034307>
- Najafi, Z., Schwartz, B. F., Chandy, A. J., & Mahajan, A. M. (2018). A two-dimensional numerical study of peristaltic contractions in obstructed ureter flows. *Computer Methods in Biomechanics and Biomedical Engineering*, 20(1), 22–32. <https://doi.org/10.1080/10255842.2017.1415333>
- O’Grady, F., & Pennington, J. H. (1966). Bacterial growth in an in vitro system simulating conditions in the urinary bladder. *British Journal of Experimental Pathology*, 47(2), 152–157.
- Ohlson, L. (1989). Morphological dynamics of ureteral transport. ii. Peristaltic patterns in relation to flow rate. *American Journal of Physiology-Regulatory, Integrative and Comparative Physiology*, 256(1), R29–R34. <https://doi.org/10.1152/ajpregu.1989.256.1.R29>
- Olweny, E. O., Portis, A. J., Afane, J. S., Brewer, A. V., Shalhav, A. L., Luszczynski, K., McDougall, E. M., & Clayman, R. V. (2000). Flow characteristics of 3 unique ureteral stents: Investigation of a poiseuille flow pattern. *Journal of Urology*, 164(6), 2099–2103. [https://doi.org/10.1016/S0022-5347\(05\)66977-7](https://doi.org/10.1016/S0022-5347(05)66977-7)
- Pozrikidis, C. (1987). A study of peristaltic flow. *Journal of Fluid Mechanics*, 180, 515–527. <https://doi.org/10.1017/S0022112087001939>
- Ramachandra, M., Mosayyebi, A., Carugo, D., & Somani, B. K. (2020). Strategies to improve patient outcomes and qol: Current complications of the design and placements of ureteric stents. *Research and Reports in Urology*, 12, 303–314. <https://doi.org/10.2147/RRU.S233981>
- Ramstedt, M., Ribeiro, I. A. C., Bujdakova, H., Mergulhão, F. J. M., Jordao, L., Thomsen, P., Alm, M., Burmølle, M., Vladkova, T., Can, F., Reches, M., Riool, M., Barros, A., Reis, R. L., Meaurio, E., Kikhney, J., Moter, A., Zaat, S. A. J., & Sjollem, J. (2019). Evaluating efficacy of antimicrobial and antifouling materials for urinary tract medical devices: Challenges and recommendations. *Macromolecular Bioscience*, 19(5), 1800384. <https://doi.org/10.1002/mabi.201800384>
- Rasouly, H. M., & Lu, W. (2013). Lower urinary tract development and disease. *WIREs Systems Biology and Medicine*, 5(3), 307–342. <https://doi.org/10.1002/wsbm.1212>
- Rassoli, A., Shafiq, M., Seddighi, A., Daneshparvar, H., & Fatouraee, N. (2014). Biaxial mechanical properties of human ureter under tension. *Urology Journal*, 11(3), 1678–1686.
- Rath, H., & Reese, G. (1984). Peristaltic flow of non-newtonian fluids containing small spherical particles. *Archives of Mechanics*, 36(2), 263–277.
- Rattner William, H., Fink, S., & Murphy John, J. (1957). Pressure studies in the human ureter and renal pelvis. *Journal of Urology*, 78(4), 359–362. [https://doi.org/10.1016/S0022-5347\(17\)66448-6](https://doi.org/10.1016/S0022-5347(17)66448-6)
- Razavi, S. E., & Jouybar, M. (2018). Fluid-structure interaction simulation of ureter with vesicoureteral reflux and primary obstructed megaureter. *Bio-medical Materials and Engineering*, 29(6), 821–837.
- Riaz, A., & Sadiq, M. A. (2020). Particle-fluid suspension of a non-newtonian fluid through a curved passage: An application of urinary tract infections. *Frontiers in Physics*, 8, 109.
- Ringel, A., Richter, S., Shalev, M., & Nissenkorn, I. (2000). Late complications of ureteral stents. *European Urology*, 38(1), 41–44. <https://doi.org/10.1159/000020250>
- Roos, R., & Lykoudis, P. S. (1971). The fluid mechanics of the ureter with an inserted catheter. *Journal of Fluid Mechanics*, 460(4), 625–630. <https://doi.org/10.1017/S0022112071000752>
- Rusconi, R., & Stocker, R. (2015). Microbes in flow. *Current Opinion in Microbiology*, 25, 1–8. <https://doi.org/10.1016/j.mib.2015.03.003>
- Sali, G. M., & Joshi, H. B. (2020). Ureteric stents: Overview of current clinical applications and economic implications. *International Journal of Urology*, 27(1), 7–15. <https://doi.org/10.1111/iju.14119>
- Salta, M., Capretto, L., Carugo, D., Wharton, J. A., & Stokes, K. R. (2013). Life under flow: A novel microfluidic device for the assessment of anti-biofilm technologies. *Biomicrofluidics*, 7(6), 064118. <https://doi.org/10.1063/1.4850796>
- Sampaio, F. J. B., Pereira-Sampaio, M. A., & Favorito, L. A. (1998). The pig kidney as an endourologic model: Anatomic contribution. *Journal of Endourology*, 12(1), 45–50. <https://doi.org/10.1089/end.1998.12.45>
- Schaeffer, A. J., Kurtz, M. P., Logvinenko, T., McCartin, M. T., Prabhu, S. P., Nelson, C. P., & Chow, J. S. (2016). Mri-based reference range for the renal pelvis anterior-posterior diameter in children ages 0–19 years. *The British Journal of Radiology*, 89(1067), 20160211. <https://doi.org/10.1259/bjr.20160211>
- Schäfer, W., Abrams, P., Liao, L., Mattiasson, A., Pesce, F., Spangberg, A., Sterling, A. M., Zinner, N. R., & Kerrebroeck, P. V. (2002). Good urodynamic practices: Uroflowmetry, filling cystometry, and pressure-flow studies**. *Neurourology and Urodynamics*, 21(3), 261–274. <https://doi.org/10.1002/nau.10066>
- Schlick, R. W., & Planz, K. (1998). In vitro results with special plastics for biodegradable endoureteral stents. *J. Endourol*, 12(5), 451–455. <https://doi.org/10.1089/end.1998.12.451>
- Scotland, K. B., Lo, J., Grgic, T., & Lange, D. (2019). Ureteral stent-associated infection and sepsis: Pathogenesis and prevention: A review. *Biofouling*, 35(1), 117–127. <https://doi.org/10.1080/08927014.2018.1562549>

- Shao, Y., Shen, Z.-J., Zhuo, J., Liu, H.-T., Yu, S.-Q., & Xia, S.-J. (2009). The influence of ureteral stent on renal pelvic pressure in vivo. *Urological Research*, 37(4), 221–225. <https://doi.org/10.1007/s00240-009-0199-z>
- Shaw, G. L., Choong, S. K., & Fry, C. (2005). Encrustation of biomaterials in the urinary tract. *Urological Research*, 33(1), 17–22. <https://doi.org/10.1007/s00240-004-0423-9>
- Sherman, E., Bayles, K., Moormeier, D., Endres, J., & Wei, T. (2019). Observations of shear stress effects on *Staphylococcus aureus* biofilm formation. *mSphere*, 4(4), e00372–e00319. <https://doi.org/10.1128/mSphere.00372-19>
- Shilo, Y., Modai, J., Leibovici, D., Dror, I., & Berkowitz, B. (2020). The impact of ureteral deformation and external ureteral pressure on stent failure in extrinsic ureteral obstruction: An in vitro experimental study. *Journal of Endourology*, 34(1), 68–73. <https://doi.org/10.1089/end.2019.0465>
- Siggers, J. H., Waters, S., Wattis, J., & Cummings, L. (2009). Flow dynamics in a stented ureter. *Mathematical Medicine and Biology*, 26(1), 1–24. <https://doi.org/10.1093/imammb/dqn020>
- Sokolis, D. P. (2019). In vitro study of age-related changes in human ureteral failure properties according to region, direction, and layer. *Proceedings of the Institution of Mechanical Engineers. Part H*, 233(5), 570–583.
- Sokolis, D. P. (2020). Alterations with age in the biomechanical behavior of human ureteral wall: Microstructure-based modeling. *Journal of Biomechanics*, 109, 109940. <https://doi.org/10.1016/j.jbiomech.2020.109940>
- Sokolis, D. P., Petsepe, D. C., Papadodima, S. A., & Kourkoulis, S. K. (2017). Age- and region-related changes in the biomechanical properties and composition of the human ureter. *Journal of Biomechanics*, 51, 57–64. <https://doi.org/10.1016/j.jbiomech.2016.11.067>
- Soria, F., Morcillo, E., Serrano, A., Budia, A., Fernández, I., Fernández-Aparicio, T., & Sanchez-Margallo, F. M. (2018). Evaluation of a new design of antireflux-biodegradable ureteral stent in animal model. *Urology*, 115, 59–64. <https://doi.org/10.1016/j.urology.2018.02.004>
- Spirka, T. A., & Damaser, M. S. (2007). Modeling physiology of the urinary tract. *Journal of Endourology*, 21(3), 294–299. <https://doi.org/10.1089/end.2007.9942>
- Stoller, M. L., Schwartz, B. F., Frigstad, J. R., Norris, L., Park, J. B., & Magliochetti, M. J. (2000). An in vitro assessment of the flow characteristics of spiral-ridged and smooth-walled jj ureteric stents. *BJU International*, 85(6), 628–631. <https://doi.org/10.1046/j.1464-410x.2000.00489.x>
- Sydney Gladman, A., Matsumoto, E. A., Nuzzo, R. G., Mahadevan, L., & Lewis, J. A. (2016). Biomimetic 4d printing. *Nature Materials*, 15(4), 413–418. <https://doi.org/10.1038/nmat4544>
- Takaddus, A. T., & Chandy, A. J. (2018). A three-dimensional (3d) two-way coupled fluid-structure interaction (fsi) study of peristaltic flow in obstructed ureters. *International Journal for Numerical Methods in Biomedical Engineering*, 34(10), e3122. <https://doi.org/10.1002/cnm.3122>
- Takaddus, A. T., Gautam, P., & Chandy, A. J. (2018). A fluid-structure interaction (fsi)-based numerical investigation of peristalsis in an obstructed human ureter. *International Journal for Numerical Methods in Biomedical Engineering*, 34(9), e3104. <https://doi.org/10.1002/cnm.3104>
- Tang, J. (2017). Microbiome in the urinary system—A review. *AIMS Microbiology*, 3(2), 143–154. <https://doi.org/10.3934/microbiol.2017.2.143>
- Tong, J. C. K., Sparrow, E. M., & Abraham, J. P. (2006). Numerical simulation of the urine flow in a stented ureter. *Journal of Biomechanical Engineering*, 129(2), 187–192. <https://doi.org/10.1115/1.2472381>
- Toro, E. F., & Siviglia, A. (2013). Flow in collapsible tubes with discontinuous mechanical properties: Mathematical model and exact solutions. *Communications in Computational Physics*, 13(2), 361–385. <https://doi.org/10.4208/cicp.210611.240212a>
- Tunney, M. M., Bonner, M. C., Keane, P. F., & Gorman, S. P. (1996). Development of a model for assessment of biomaterial encrustation in the upper urinary tract. *Biomaterials*, 17(10), 1025–1029. [https://doi.org/10.1016/0142-9612\(96\)84679-5](https://doi.org/10.1016/0142-9612(96)84679-5)
- Vahidi, B., & Fatourae, N. (2007). A numerical simulation of peristaltic motion in the ureter using fluid structure interactions. In *29th Annual International Conference of the IEEE Engineering in Medicine and Biology Society*, pp. 1168–1171.
- Vahidi, B., & Fatourae, N. (2012). A biomechanical simulation of ureteral flow during peristalsis using intraluminal morphometric data. *Journal of Theoretical Biology*, 298, 42–50. <https://doi.org/10.1016/j.jtbi.2011.12.019>
- Vahidi, B., Fatourae, N., Imanparast, A., & Moghadam, A. N. (2011). A mathematical simulation of the ureter: Effects of the model parameters on ureteral pressure/flow relations. *Journal of Biomechanical Engineering*, 133(3), 031004. <https://doi.org/10.1115/1.4003316>
- Venkatesh, R., Landman, J., Minor, S. D., Lee, D. I., Rehman, J., Vanlangendonck, R., Ragab, M., Morrissey, K., Sundaram, C. P., & Clayman, R. V. (2005). Impact of a double-pigtail stent on ureteral peristalsis in the porcine model: Initial studies using a novel implantable magnetic sensor. *Journal of Endourology*, 19(2), 170–176. <https://doi.org/10.1089/end.2005.19.170>
- Villanueva, C. A., Nelson, C. A., & Stolle, C. (2015). Intravesical tunnel length to ureteral diameter ratio insufficiently explains ureterovesical junction competence: A parametric simulation study. *Journal of Pediatric Urology*, 11(3), 144. e1–144. e5. <https://doi.org/10.1016/j.jpuro.2015.01.015>
- Villanueva, C. A., Tong, J., Nelson, C., & Gu, L. (2018). Ureteral tunnel length versus ureteral orifice configuration in the determination of ureterovesical junction competence: A computer simulation model. *Journal of Pediatric Urology*, 14(3), 258. e1–258. e6. <https://doi.org/10.1016/j.jpuro.2018.01.009>
- Walzak, M. P., & Paquin, A. J. (1961). Renal pelvic pressure levels in management of nephrostomy. *The Journal of Urology*, 85(5), 697–702. [https://doi.org/10.1016/S0022-5347\(17\)65410-7](https://doi.org/10.1016/S0022-5347(17)65410-7)

- Waters, S., Heaton, K., Siggers, J., Bayston, R., Bishop, M., Cummings, L., Grant, D., Oliver, J., & Wattis, J. (2008). Ureteric stents: Investigating flow and encrustation. *Proceedings of the Institution of Mechanical Engineers, Part H: Journal of Engineering in Medicine*, 222(4), 551–561.
- Weinberg, S. R., & Maletta, T. J. (1961). Measurement of peristalsis of the ureter and its relation to drugs. *JAMA*, 175(1), 15–18. <https://doi.org/10.1001/jama.1961.03040010017005>
- Wolf, J. S., Humphrey, P. A., Rayala, H. J., Gardner, S. M., Mackey, R. B., & Clayman, R. V. (1996). Comparative ureteral microanatomy. *Journal of Endourology*, 10(6), 527–531. <https://doi.org/10.1089/end.1996.10.527>
- Yin, F. C., & Fung, Y. C. (1971). Mechanical properties of isolated mammalian ureteral segments. *The American Journal of Physiology*, 221(5), 1484–1493.
- Zalewska-Piatek, B., Olszewski, M., Lipniacki, T., Błoński, S., Wiczór, M., Bruździak, P., Skwarska, A., Nowicki, B., Nowicki, S., & Piatek, R. (2020). A shear stress micromodel of urinary tract infection by the *Escherichia coli* producing dr adhesin. *PLoS Pathog*, 16(1), e1008247. <https://doi.org/10.1371/journal.ppat.1008247>
- Zelenko, N., Coll, D., Rosenfeld, A. T., & Smith, R. C. (2004). Normal ureter size on unenhanced helical ct. *American Journal of Roentgenology*, 182(4), 1039–1041. <https://doi.org/10.2214/ajr.182.4.1821039>
- Zhu, Y., Yang, K., Cheng, R., Xiang, Y., Yuan, T., Cheng, Y., Sarmiento, B., & Cui, W. (2017). The current status of biodegradable stent to treat benign luminal disease. *Materials Today*, 20(9), 516–529. <https://doi.org/10.1016/j.mattod.2017.05.002>
- Zien, T. F., & Ostrach, S. (1970). A long wave approximation to peristaltic motion. *Journal of Biomechanics*, 3(1), 63–75. [https://doi.org/10.1016/0021-9290\(70\)90051-5](https://doi.org/10.1016/0021-9290(70)90051-5)
- Zimskind Paul, D., Fetter Theodore, R., & Wilkerson, J. L. (1967). Clinical use of long-term indwelling silicone rubber ureteral splints inserted cystoscopically. *Journal of Urology*, 97(5), 840–844. [https://doi.org/10.1016/S0022-5347\(17\)63130-6](https://doi.org/10.1016/S0022-5347(17)63130-6)

How to cite this article: Zheng S, Carugo D, Mosayyebi A, et al. Fluid mechanical modeling of the upper urinary tract. *WIREs Mech Dis*. 2021;e01523. <https://doi.org/10.1002/wsbm.1523>

APPENDIX

The value of various parameters used in previous UUT models are given in the following tables, along with the physiological range taken from clinical references as detailed in Section 2. One may use these tables to find out which cases have been investigated before, and fill in the gaps with new UUT models for other patho-physiological conditions.

Tables A1–A5

TABLE A1 Checklist of previous studies of urinary tract using different modeling methods on various physiological and pathological conditions

	Reduced models	Computational models	Experimental models
Peristalsis	Zien and Ostrach (1970), Lykoudis and Roos (1970), Roos and Lykoudis (1971), Mitra and Prasad (1973), Rath and Reese (1984), Pozrikidis (1987), Griffiths (1987), Griffiths et al. (1987), Griffiths (1989), Hariharan et al. (2008), Jiménez-Lozano (2009), Jiménez-Lozano et al. (2011), Toro and Siviglia (2013), Riaz and Sadiq (2020)	Vahidi and Fatourae (2007), Vahidi et al. (2011), Vahidi and Fatourae (2012), Takaddus and Chandy (2018), Takaddus et al. (2018), Najafi et al. (2018)	Graw and Engelhardt (1986)
Ureter geometry	Riaz and Sadiq (2020)	Kim et al. (2015a, 2015b), Kim et al. (2017b), Razavi and Jouybar (2018)	Kim, Kim, Choi, Lee, and Baba (2020)
Body movement			Stoller et al. (2000)
Multiphase flow	Rath and Reese (1984), Jiménez-Lozano (2009), Jiménez-Lozano and Sen (2010), Jiménez-Lozano et al. (2011), Riaz and Sadiq (2020)	Chrispell and Fauci (2011)	
Non-Newtonian flow	Rath and Reese (1984), Riaz and Sadiq (2020), Hariharan et al. (2008)	Chrispell and Fauci (2011)	
VUR	Cummings et al. (2004), Waters et al. (2008), Siggers et al. (2009)	Razavi and Jouybar (2018)	
Internal obstruction	Siggers et al. (2009)	Tong et al. (2006), Carugo et al. (2014), Clavica et al. (2014), Najafi et al. (2016), Kim et al. (2017a), Najafi et al. (2018), Takaddus and Chandy (2018), Takaddus et al. (2018)	Carugo et al. (2013), Clavica et al. (2014)
External obstruction			Hofmann and Hartung (1989)
Stent configuration	Cummings et al. (2004)	Kim et al. (2015a, 2015b), Kim et al. (2017a), Kim, Kim, Choi, Lee, Baba, and Suh (2020)	Graw and Engelhardt (1986), Lange et al. (2011), Stoller et al. (2000), Olweny et al. (2000), Hofmann and Hartung (1989)
Encrustations and bacterial growth	Waters et al. (2008)		Gorman et al. (2003), Choong et al. (2000), Tunney et al. (1996), O'Grady and Pennington (1966)

(Continues)

TABLE A1 (Continued)

	Reduced models	Computational models	Experimental models
Interluminal flow	Cummings et al. (2004), Siggers et al. (2009)	Tong et al. (2006), Clavica et al. (2014), Kim et al. (2015a, 2015b)	Stoller et al. (2000), Carugo et al. (2013), Clavica et al. (2014)
Cavity flow		Clavica et al. (2014), De Grazia et al. (2020)	Clavica et al. (2014)
Single side hole geometry		Mosayyebi et al. (2019)	Mosayyebi, Yue, et al. (2018); Mosayyebi et al. (2019)
Microparticle accumulation	Jiménez-Lozano (2009), Jiménez-Lozano and Sen (2010), Jiménez-Lozano et al. (2011)	Mosayyebi et al. (2019)	Cauda et al. (2017), Laffite et al. (2016), Mosayyebi, Yue, et al. (2018); Mosayyebi et al. (2019), Kim, Olympiou, McCoy, Irwin, and Rimer (2020)
Bacterial attachment	Jiménez-Lozano (2009), Jiménez-Lozano and Sen (2010), Jiménez-Lozano et al. (2011)	De Grazia et al. (2020)	Hobbs et al. (2018), De Grazia et al. (2020)

TABLE A2 Dimensions and material properties of the ureter from clinical references and previous studies

	Length (mm)	Internal diameter (mm)	Wall thickness (mm)	Distensibility (cmH₂O/mm)	Stiffness (cmH₂O/ mm)	Elastic modulus (kPa)
Clinical reference	220–300	1.8 (1–6)	~1	2.04		3480 ± 470 (longitudinal) 2310 ± 460 (circumferential)
Lykoudis and Roos (1970)		3				
Roos and Lykoudis (1971)		1–2				
Griffiths (1989)				2.04		
Cummings et al. (2004) ^a	250	4 (≤6)			41–45	
Bykova and Regirer (2005)	300–350					
Tong et al. (2006)		2.8–3				
Siggers et al. (2009)	250	4				
Vahidi et al. (2011)		9				5, 10
Bevan et al. (2012)	300	0.4	0.75			500
Carugo et al. (2013) ^a	289 ± 20	2.2–6.5				
Kim et al. (2015a)	226.21	3, 4.57				
Kim et al. (2015b)	226.21	4.57				
Villanueva et al. (2015)		3–30	0.2–3			
Gómez-Blanco et al. (2016)	280					
Takaddus and Chandy (2018)	10	2				10 ¹⁰
Mosayyebi et al. (2019)	60	1.9–5.3				
Kim, Kim, Choi, Lee, Baba, and Suh (2020)	226.21	3.59–5.69				
Kim, Kim, Choi, Lee, and Baba (2020)	226.21	4.57, 3.59–5.69				

^aData obtained from porcine model.

TABLE A3 Typical pressure conditions and flow rates associated with the urinary system from clinical references and previous studies

	Resting pressure (cmH ₂ O)	Ureter inlet pressure (cmH ₂ O)	Ureter outlet pressure (cmH ₂ O)	Voiding pressure (cmH ₂ O)	Peristalsis wave speed (cm/s)	Flow rate (ml/min)
Clinical reference	8	12–15	2–5	≥20	2–3	
Lykoudis and Roos (1970)	5.4			40.79	3	
Griffiths (1987)				30	3	
Cummings et al. (2004) ^a	4	4, 20 ^a	2 – 5	30, 50		0.5, 4 (diabete)
Bykova and Regirer (2005)				20.4–27.2		
Siggers et al. (2009)		4				0.5
Alloussi et al. (2010)				38.3 ± 11.5 (male) 32 ± 10.6 (female)		
Vahidi et al. (2011)						
Kim et al. (2011)						
Bevan et al. (2012)						0.57 (0.29 – 0.92)
Carugo et al. (2013) ^a						
Kim et al. (2015a)		0.5, 1, 2	0			
Kim et al. (2015b)		0.5	0			0.38, 2.08
Gómez-Blanco et al. (2016)	5.4	6.8 ^a	2.7			
Mosayyebi et al. (2019)						1 (0.8–1.5)
Kim, Kim, Choi, Lee, Baba, and Suh (2020)		1	0			0.21, 0.275
Kim, Kim, Choi, Lee, and Baba (2020)		20	4			167–667

^aData obtained from porcine model.

TABLE A4 Parameters of various stent configurations that have been previously studied

	Length (mm)	Outer diameter (mm)	Internal diameter (mm)	Angular arrangement of SH (°)	SH radius (mm)	Vertex angle (°)	Number of SH (N)
Cummings et al. (2004)	250		2		0.25		50
Tong et al. (2006)	246	2		90, 180			0, 11, 17
Waters et al. (2008)	250	2	1.3		0.25		
Siggers et al. (2009)		1.9	1.3				
Kim et al. (2015a)		2	1	90, 180	0.5		0, 11, 22
Kim et al. (2015b)				45, 90, 180			11, 45
Cauda et al. (2017)	260	1.5, 2.0	1.24				
Mosayyebi et al. (2019)	180, 400		12.5		0.240.5	45, 90, 120	
Kim, Kim, Choi, Lee, Baba, and Suh (2020)		2		0, 90, 180, 270			16, 32, 45
Kim, Kim, Choi, Lee, and Baba (2020)	240	1.67–2.67	1–1.67	45, 90, 180	0.5		0, 11, 23, 47

Note: Angular arrangement prescribes the angular location of side holes along the longitudinal axis. SH stands for side hole. Vertex angle defines the vertex angle of the stent wall at the side hole opening.

TABLE A5 Material properties of artificial urine from clinical references and previous studies

	Kinematic viscosity (cm ² /s)	Dynamic viscosity (g/cm s)	Density (g/cc)	pH
Clinical reference	0.0083 (37°C) 0.0069 (42°C)	0.011	0.99	~6
Lykoudis and Roos (1970)	0.007			
Griffiths (1987)		0.01		
Schlick and Planz (1998)				7.9 (5–9)
Choong et al. (2000)				6
Cummings et al. (2004)		0.00654	1	
Waters et al. (2008)		0.00654	1	
Siggers et al. (2009)		0.00654	1	
Vahidi et al. (2011)		0.013	1.05	
Carugo et al. (2014)		0.01	1	
Kim et al. (2015b)		0.00654	1.003	
Takaddus and Chandy (2018)		0.013	1.05	
Hobbs et al. (2018)				6.8–8.8
Mosayyebi, Manes, et al. (2018)				6.8
Mosayyebi et al. (2019)		0.01	0.997	
Kim, Kim, Choi, Lee, Baba, and Suh (2020)		0.00654	1003	